Fault Detection and Location of DC Microgrids

Bayati, Navid

Publication date:
2020

Document Version
Publisher's PDF, also known as Version of record

FAULT DETECTION AND LOCATION OF DC MICROGRIDS

BY
NAVID BAYATI

DISSERTATION SUBMITTED 2020

AALBORG UNIVERSITY
DENMARK

Fault Detection and Location of DC Microgrids

Ph.D. Dissertation

Navid Bayati

Aalborg University

Department of Energy Technology

Dissertation submitted: October 2020

PhD supervisor: Associate Professor Amin Hajizadeh
Aalborg University

Assistant PhD supervisor: Associate Professor Mohsen N. Soltani
Aalborg University

PhD committee: Associate Professor Jayakrishnan Radhakrishna Pillai (chair)
Aalborg University

Professor Francisco Gonzalez-Longatt
University of South Eastern Norway

Associate Professor Mehdi Savaghebi
University of Southern Denmark

PhD Series: Faculty of Engineering and Science, Aalborg University

Department: Department of Energy Technology

ISSN (online): 2446-1636
ISBN (online): 978-87-7210-824-7

Published by:
Aalborg University Press
Kroghstræde 3
DK – 9220 Aalborg Ø
Phone: +45 99407140
aauf@forlag.aau.dk
forlag.aau.dk

Printed in Denmark by Rosendahls, 2020

Preface:

This Ph.D dissertation entitled “Fault Detection and Location of DC Microgrids” has been submitted to the Doctoral School of Aalborg University, in partial fulfillment of the requirement of the Ph.D degree.

All researches are carried out at the Department of Energy Technology, Aalborg University, Esbjerg from November 2017 to November 2020 under supervision of Amin Hajizadeh and co-supervision of Mohsen Soltani.

This dissertation has been submitted in the partial fulfillment of the Ph.D degree. The thesis is based on the published and submitted papers, and parts of the papers are used directly or indirectly in the thesis. The present form of the thesis cannot be openly published, only limited and closed circulation as copyright may not be ensured.

Navid Bayati

Abstract

In recent years, by increasing the penetration of renewable energy sources (RESs), the development of power electronic converters, and environmental concerns, the utilizing of DC Microgrids has been dramatically increased. However, besides the advantages of DC Microgrids over AC systems, the protection of these systems has not been significantly studied and developed. Therefore, this work proposed and suggested localized fault detection and location schemes for DC Microgrids with both radial and ring configurations during islanded and grid-connected modes. Furthermore, the different types of loads, such as constant power loads (CPLs), DC motors, and DC resistive loads are considered and the impact of CPLs on the protection of DC Microgrids is investigated. In addition, due to eliminating the communication links in the proposed protection system, the cost and reliability of DC Microgrid protection systems are improved. On the other hand, for providing more power support and better reliability, the concept of DC Microgrid cluster has been presented in recent years. However, there is a lack of study on the protection of these systems. This work also proposes several fault detection and location schemes for these systems based on different transient signal processing tools. The proposed schemes are tested by simulation in MATLAB and Digsilent, and by experimentation by dSPACE. The results of the suggested protection scheme are shown during different scenarios such as high impedance fault, overload, noise, and bad calibration. The outcome of this work proves the effectiveness of the proposed local fault detection and location scheme on both DC Microgrids and DC Microgrid clusters.

Abstrakt

I de senere år er brugen af DC-mikronet blevet øget på grund af stigningen i penetrationen af vedvarende energikilder (RES), udviklingen af elektroniske kraftomformere og miljøhensyn. På trods af fordelene ved DC Microgrids i forhold til AC-systemer er beskyttelsen af disse systemer ikke blevet undersøgt og udviklet signifikant. Derfor foreslog denne ph.d.-afhandling lokaliserede fejldetekterings- og placeringsskemaer for DC-mikronetværk med både radial og ringkonfiguration under ø-og net-tilsluttet tilstande. Desuden overvejes de forskellige typer belastninger, såsom konstant effektbelastninger (CPL'er), jævnstrømsmotorer og jævnstrømsmodstandsbelastninger, og CPL'ernes indvirkning på beskyttelsen af jævnstrømsnetværk undersøges. Desuden forbedres omkostningerne og pålideligheden af DC Microgrid-beskyttelsessystemer på grund af eliminering af kommunikationslinkene i det foreslåede beskyttelsessystem. For at give mere support og bedre pålidelighed er konceptet med DC Microgrid-klynge præsenteret i de seneste år. Der mangler dog undersøgelse af beskyttelsen af disse systemer. Dette arbejde foreslår også flere fejlregistrerings- og lokaliseringsskemaer for disse systemer baseret på forskellige hurtige signalbehandlingsværktøjer. De foreslåede ordninger testes ved simulering i MATLAB og Digsilent og ved eksperimentering med dSPACE. Resultaterne af den foreslåede beskyttelsesordning vises under forskellige scenarier såsom højimpedansfejl, overbelastning, støj og dårlig kalibrering. Resultatet af dette arbejde beviser effektiviteten af den foreslåede lokale fejldetektering og lokaliseringsplan på både DC Microgrids og DC Microgrid klynger.

Acknowledgment

At First, I would like to express my great gratitude to my supervisor, Associate Professor Amin Hajizadeh for all trust and helps given to me to pursue a Ph.D. He always inspired and encourage me with new ideas during this journey. He has not been only an advisor also as a friend making the work environment more pleasant for me. Also, I am highly indebted to my co-supervisor, Associate Professor Mohsen Soltani, for help, supports, and valuable comments to ensure the success of my researches on this Ph.D. study.

I sincerely thank my friends and colleagues, Meisam Sadi, Mehdi Nikbakht Fini, Omid Lorzadeh, and Mojtaba Yousefi for making enlivening, and interesting times on my Ph.D. journey.

I also like to thank Dr. Zhengyu Lin and their team, CREST, at Loughborough University in England for hosting me during study abroad. Thanks for the hospitality of the CREST team and for making a successful scientific research for me.

At the end, I would like to say a huge thanks to my family from the bottom of my heart. Thanks, Fateme, my love and wife, for encouraging me with her patience and kindness through this way. But most of all, thank you for being my best friend. Thanks my mother, Tahereh, and my father, Ebrahim, for trusting me on my ideas and guiding me during tough moments. Also thanks my brother, Nima, for helping me with my entire life.

I would like to thank God for giving me the strength, and knowledge to undertake this research study and to persevere and complete it satisfactorily. Without his blessings, this achievement would not have been possible.

Contents

Chapter 1

Introduction

This chapter gives an introduction, background, motivation, and aims of this thesis.

1.1.Background and Motivation

Developments in power electronic converters, energy storage devices, renewable energy sources (RESs), and modern control strategies lead to implementing and increasing the penetration of DC Microgrids in power distribution systems [1]. In DC Microgrids, different types of RESs such as microturbines, wind turbines (WTs), fuel cells (FCs), and photovoltaic (PV) arrays produce power with different types of electricity, AC or DC, and frequencies. Therefore, power electronic converters are essential in these systems to connecting all RESs [2]. Because the nature of the majority of loads is DC, in DC Microgrids, DC loads and RESs can connect to a common DC bus with fewer conversion stages. Therefore, it results in fewer power losses and costs compared to AC Microgrids. In summary, the advantages of DC Microgrids over AC systems can be presented as

- The majority of residential loads are DC or can be operated by DC voltage.
- AC and DC systems require six and two current leads, respectively, that can reduce losses in DC microgrids, and thus lower refrigeration and cost [3].

- Lack of skin effect in DC cables, then, the power losses in cables decrease by 15–20% [4].
- More safety of DC systems for human bodies [5].
- Higher power transfer capacity [5].
- Fewer conversion stages reduce the power losses and heat because the majority of loads and resources are DC [6].
- The majority of the storage devices such as battery and ultra-capacitors are DC [7].
- Due to the lack of frequency and phase in DC systems, synchronization problems are eliminated in DC Microgrids [8].

DC Microgrids are implemented and considered in several applications by two different voltage levels, low voltage (LV) and medium voltage (MV). Typically, in shipboard and maritime DC Microgrids, the MV level is considered, rated from 1.5 kV to 22 kV, since it enables to prepare energy and power density of maritime systems [9]-[10]. On the other hand, the LVDC Microgrids are used in wide applications such as residential, electric vehicles, and telecom systems [11]-[13]. Moreover, in the case of urban DC Microgrids, for improving the power support and management, several DC Microgrids can be connected to make a DC Microgrid cluster [14].

It is undeniable fact that after the recent technical developments in the power electronic converters, DC systems had wide attention. Due to these developments, DC/DC and AC/DC converters with more flexibility in variously rated voltages are widely implemented in DC systems [15]. However, the availability of converters causes more penetration of RESs in DC Microgrids by higher numbers of point of common coupling (PCC), which

causes the need for more complex and smart protection, control, and management systems to ensure reliable and safe operation of DC Microgrid.

Based on the above explanations, the DC Microgrids have advantages over conventional AC systems, however, they have associated with some protection problems. The lack of zero-crossing point, fast high rise fault current performance, lower tolerant of power electronic devices, and lack of proper protection standards cause the require of fast fault detection in these systems, also, during high impedance faults (HIFs), the requirements of a HIF location scheme will be essential. Furthermore, due to the cost, noise, delay, and packet dropout of communication infrastructures, eliminating the communication link in protection systems greatly improve the performance of protection systems. Then, the lack of improved protection systems for DC Microgrids is a barrier to the wide DC implementation at distribution levels. A well-designed protection system guarantees reliable operation with high security and dependability of a DC Microgrid.

1.2.Overview, Hypothesis, and Aims

The introduction of RESs a formation of DC Microgrids has a profound effect on the performance and operation of protection systems, and it makes new requirements to satisfy the safety and reliability of the system [16]. In particular, the nature of a DC Microgrid requires a fast and reliable protection system capable of detecting and locating both LIFs and HIFs. Moreover, the majority of existing protection systems utilize the communication link to use the measured values of both sides of each line to detect and locate faults. However, the implementation of communication links increases cost, delay, noise, failure probability, and packet dropout, which dramatically decreases the effectivity of the protection system. Consequently, avoiding communication links improves the reliability and cost of DC Microgrids.

On the other hand, during the HIFs, due to the small change of fault current, the detecting and locating of HIFs and also distinguishing overload and fault current are challenging problems. Therefore, the protection system should be equipped with a HIF detection and location function to protect the system during these types of faults.

In DC Microgrids, several different types of loads are installed, such as DC motor, resistive loads, and constant power loads (CPLs). However, the existing studies neglected the impact of CPLs on protection systems. Therefore, since the majority of loads are CPLs and they have a different system behavior during faults, it is essential to also implement the CPL protection system in DC Microgrids.

Based on the aforementioned issues and challenges, the aims with this project are:

- to investigate the impact of CPLs during fault and propose a CPL protection system,
- to detect faults in mesh DC Microgrids within the lowest possible time without using communication links,
- to locate both LIFs and HIFs in DC Microgrids by local measured values by highest accuracy,
- to investigate the behavior of DC Microgrid clusters during fault and propose a local protection system for them,

1.3.Outline of the Papers

The thesis is constructed as summary, based on the contribution of published/submitted papers. The main contribution of this thesis is based on the researches prepared in the following manuscripts:

Journal papers:

JP1: N. Bayati, A. Hajizadeh and M. Soltani, "Protection in DC microgrids: a comparative review," in IET Smart Grid, vol. 1, no. 3, pp. 66-75, 10 2018, DOI: 10.1049/iet-stg.2018.0035.

JP2: N. Bayati, H. R. Baghaee, A. Hajizadeh and M. Soltani, "Localized Protection of Radial DC Microgrids With High Penetration of Constant Power Loads," in IEEE Systems Journal, DOI: 10.1109/JSYST.2020.2998059.

JP3: N. Bayati, H. R. Baghaee, A. Hajizadeh, M. Soltani, and Z. Lin, "A Fuse Saving Scheme for DC Microgrids With High Penetration of Renewable Energy Resources", in IEEE Access, 10.1109/ACCESS.2020.3012195

JP4: N. Bayati, H. R. Baghaee, A. Hajizadeh, M. Soltani, and Z. Lin, "Local Fault Location in Meshed DC Microgrids based on Parameter Estimation Technique", submitted to IEEE Systems Journal.

JP5: N. Bayati, H. R. Baghaee, A. Hajizadeh, M. Soltani, and Z. Lin, "Mathematical Morphology-based Local Fault Detection in DC Microgrid Clusters Article", submitted to Electric Power Systems Research.

JP6: N. Bayati, H. R. Baghaee, A. Hajizadeh, M. Soltani, and Z. Lin, "Local High-Impedance Fault Location Strategy for DC microgrid Clusters using SVMs", submitted to IEEE Transactions on Smart Grids.

JP7: N. Bayati, H. R. Baghaee, A. Hajizadeh, M. Soltani, and Z. Lin, "A Local High Impedance Fault Detection Scheme Using Empirical Mode Decomposition and Hilbert-Huang Transform for DC Microgrid Clusters", submitted to IEEE Journal of Emerging and Selected Topics in Power Electronics.

The chronology of the papers follows Fig. 1,

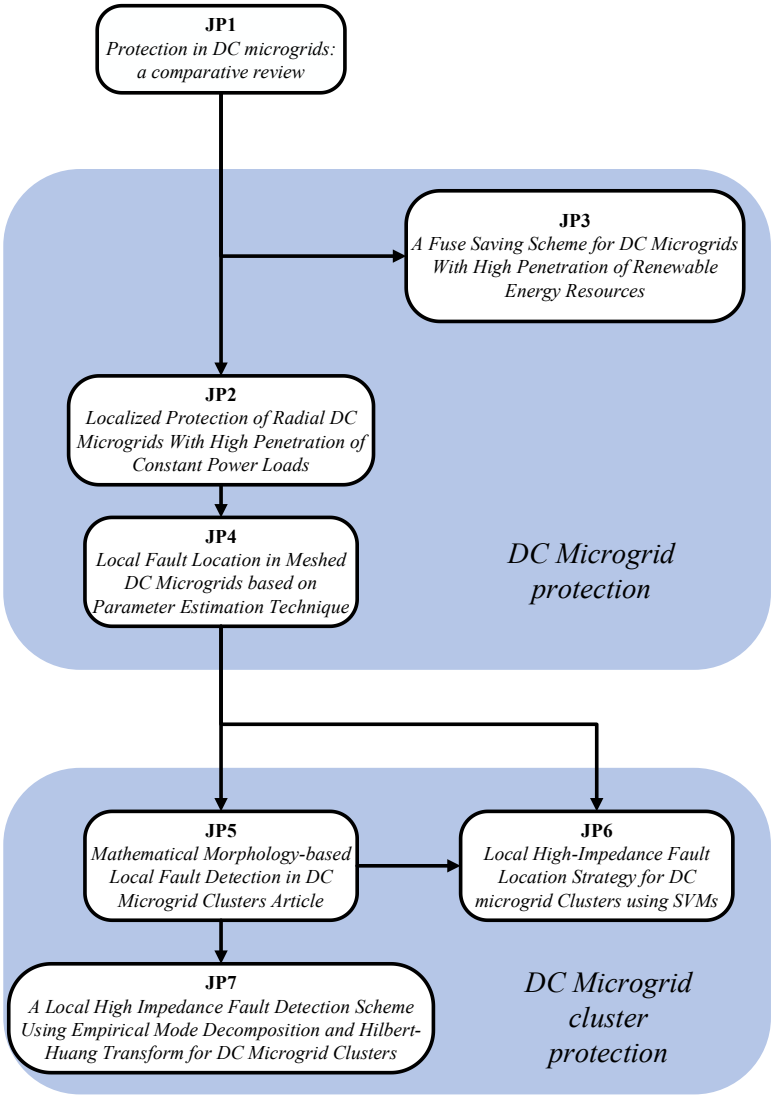

Fig. 1. Chronology of published/submitted papers

1.4. Thesis Structure

The thesis is organized into the following chapters.

Chapter 2 starts with a literature review on the protection of DC Microgrids. Then, the focus is placed on the particular requirements of DC Microgrid protection systems and on existing works. The main parts of this chapter have been presented in journal paper JP1.

Chapter 3 proposes a local fault detection scheme for both DC Microgrids and DC Microgrid clusters based on the transient behavior of fault current. In this fast fault detection scheme, faults are detected by only using the signals of the current sensor at one end of the line segment. Accordingly, the fault detection method does not rely on the communication link, and synchronized measured current from both sides of the line. The speed and other characteristics of the proposed method are compared with other methods and tested by simulations and experimentations. The main parts of this chapter have been presented in journal papers JP3, JP5, and JP7.

Chapter 4 suggests the HIF location scheme for both DC Microgrids and DC Microgrid clusters based on local measurements. The proposed strategies are designed based on the performance of each section of DC Microgrids. At the first stage, the low impedance fault (LIF) and HIF location are designed for constant power loads (CPLs). Then, the HIF location is proposed for meshed DC Microgrids by parameter estimation. Finally, the fault location of the DC Microgrid cluster is defined by using support vector machines (SVMs). All proposed works are tested and validated by experimentations and simulations, and compared with each other and other existing methods. The main parts of this chapter have been presented in journal papers JP2, JP4, and JP6.

1.5. Scientific contributions

The scientific contributions of this work are as follows:

- The behavior of different types of loads, such as DC motor, resistive load, and CPLs are tested during faults in a DC Microgrid.
- By analyzing the performance of CPLs during a fault in simulation and experimentation, a fault location method for CPLs is proposed.
- The accuracy of the CPL protection method is compared with other load protection methods.
- The performance of DC Microgrids during fault is investigated.
- A fault location and detection scheme rely on local measurement units are proposed for DC Microgrids to protect the system against both LIFs and HIFs, and validated by simulation and experimentation.
- The impact of HIFs on DC Microgrid clusters is analyzed, and a local protection system is proposed for these systems.
- An experimental setup has been built and used to show the feasibility of using proposed protection systems of DC Microgrid and DC Microgrid clusters during HIFs and LIFs by local sensors.

Chapter 2

Protection of DC Microgrids

Based on JP1, this chapter presents the detailed background and literature review of DC Microgrid protection.

2.1. Challenges of Protection of DC Microgrids

DC Microgrids faced with several challenges during faults, due to the different characteristics of DC and AC systems, the low peak time, and the high magnitude of fault current. Therefore, the first step of designing a suitable protection system for DC Microgrids is investigating the challenges and differences in DC systems.

2.1.1. The Direction of Fault Current

Typically, the topology of the traditional power systems are radial, and the fault current is unidirectional, therefore, they can be protected by traditional current-based relays [17]. Conversely, in DC Microgrids, the RESs are connected to different locations, and the system has a ring topology, therefore, the fault current is made different bidirectional currents. Consequently, the traditional protection systems cannot be directly implemented in DC Microgrids [18]. On the other hand, the topology of DC Microgrids may regularly change, thus, the direction of fault current can change. Therefore, the traditional relays, for example, directional overcurrent relays with fixed settings, cannot be implemented in these systems.

2.1.2. Non-suitability of AC Protection Devices in DC Systems

In the AC systems, the circuit breakers (C.Bs) interrupt the fault current at the zero-crossing points at every half period. However, due to the lack of zero-crossing point in DC systems, the conventional AC C.Bs cannot be implemented directly in DC Microgrids [19]. Moreover, high fault clearing time and arcing phenomena are the disadvantages of DC C.Bs. Therefore, to improve it, solid-state C.Bs (SSCBs) are widely used in the DC Microgrids, and the economic feasibility of these devices should be considered in the designing of protection systems.

Furthermore, since, the DC fault current has lower peak time and higher magnitude, DC Microgrids require a fault detection method with lower speed compared to AC systems to prevent damages to converters [20].

2.1.3. Low Fault Current Capacity of Inverters

The fault current tolerant capacity of inverters in DC Microgrids normally is less than half of the designing fault current magnitude [21]. Therefore, it is essential to detect faults within the peak time to isolate the faulty line before the peak magnitude. Moreover, during the fault, the operation mode of DC Microgrids can change to islanded mode to reduce the fault current level, however, it requires complex and dynamic coordination between protection devices such as fuses, and relays.

2.1.4. Communication Challenges

The majority of protection systems require communication infrastructures between protection devices and relays to send and analyze measured values of both ends of lines for detecting and locating faults. Therefore, they require a reliable communication link for instantaneous data transfer between relays for fault detection and location. The chances of data loss or communication failure

require a separate backup protection system. Thus, this increases the cost and size of the protection system and limits the application of DC Microgrids. Moreover, utilizing a communication link in protection systems causes noise and delay, which increases the response time and error of the protection system [22].

2.1.5. Lack of Guidelines and Standards

One of the main challenges during implementing DC Microgrids is the lack of standards and guidelines for the protection and safety of these systems. The standardizing of DC Microgrids should be developed based on the applications of these systems to help to create protection standards of different components based on the system configuration. The other parameters such as grounding schemes, protection of both grid-connected and islanded DC Microgrids are also required standardization. The general standards of fault detection and location are important, due to the affecting fault clearing time on the performance of DC Microgrids [23].

2.2.Protection Methods in DC Microgrids

Due to the nature of DC systems, such as large DC capacitors, the low impedance of DC cables, high transient current, and low peak time, the AC protection systems cannot be directly utilized in DC Microgrids [24]. Therefore, in this section, the application of different protection methods on DC Microgrids is investigated.

2.2.1. Overcurrent Protection

In this method, the same as the AC overcurrent protection method, a threshold is required to be considered to detect the fault. Moreover, the coordination between overcurrent relays in AC systems is determined based on standards, however, in DC systems, these standards cannot be used to

coordinate overcurrent relays. In [25], an overcurrent protection is utilized in a DC Microgrid, however, due to the more complexity of DC microgrids compared to AC systems, this method may result in longer fault clearance time and the disconnection of the larger zone of the system during the fault. Furthermore, in compact DC Microgrids, the time margin between downstream and upstream protection operation is small, then, the upstream relay may act faster than the downstream relay. Thus, the solution to this problem is using a communication link between relays, which also causes higher costs, and delays [26]. A framework based on the integration of unit-based protection is proposed in [27], which has high selectivity, speed, and sensitivity. Another drawback of overcurrent protection systems is the low sensitivity during HIFs.

2.2.2. Impedance-based Methods

A distance protection method for DC systems is suggested in [28], and a simple algorithm by using two measurement units at both ends of lines is presented. Moreover, in this study, the fault is located by measuring the reference voltage and estimating the fault location by the impedance of line. However, this method has a high sensitivity to the fault resistance, and HIFs reduce the accuracy of this method. These methods can be effective in fault detection schemes, however, in fault location methods, the accuracy of impedance-based methods is low.

2.2.3. Communication-based Methods

A common and well-known protection method is differential protection, which detects the fault by comparing the current magnitude and directions at two ends of the under protection unit [29]. In [30], a differential protection system is presented for DC networks with high accuracy and speed. First, both relays measure the current values and calculate the difference between them,

and if it becomes greater than a threshold, the trip signal will be sent to SSCBs. The fault resistance, RESs, fault magnitude have a low impact on the differential methods, however, due to the high dependence on the communication links, these methods are expensive and vulnerable to noise and delay [31].

2.2.4. Wavelet-based and Intelligent Methods

In [32], a wavelet-based protection system is presented for DC systems. Wavelet is an efficient method for extracting the features of transient signals. Also, the wavelet methods can be linked with intelligent methods to provide more options for protection systems, such as HIF detection, faster fault detection, and locating faults. However, the wavelet-based methods cannot directly implement in DC systems. For example, in [33], fault current measurements are sampled and wavelet transform calculates and captures the characteristic changes in the current signals caused by network faults.

2.2.5. Current Derivative Protection

After disturbances, the current derivative increase from approximately zero to a high value. Thus, it can be considered as a solution to detect the fault within milliseconds. However, it depends on the fault impedance, line loading, and cable length, then, determining a proper threshold to determining fault is an obstacle. Moreover, it is very difficult to distinguish between overload and faults in this method. Therefore, in [34], the first and second derivative orders of current are considered to detect faults. Moreover, to measure the current derivative accurately, a high sampling rate sensor is essential, and it may result in noise and false tripping.

Table 1. Table from paper JP1, comparing of protection methods according to their advantages and disadvantages

Protection method	Advantages	Disadvantages
Distance-Protection	• Simple method	• sensitive to resistance of fault • typically requires backup unit • Low accuracy in the short lines
Differential-Protection	• sensitive • Low dependency to impedance of fault • Independent to the direction of current • Independent to the raising rate current of DC systems and fault resistance	• require a high bandwidth communication link • Low accuracy with noisy measurements • require accurate and fast data synchronization
Overcurrent-Protection	• Simple method • Applicable in fault clearing approaches	• only applicable in the LV and MV systems • Should be implemented with other methods or use communication links to improve selectivity • need an accurate and fast scheme for diagnosing the current direction • Cannot detect HIFs
Wavelet	• Effective in fault detection methods • Can be applied as a hybrid method with other protection schemes	• Requires GPS • Requires data acquisition units with a high sampling rate
Current derivative protection	• Fast • Local	• Expensive • Difficult to find a threshold • Vulnerable to noise
ANN	• Can be linked to other methods • Accurate and robust	• the trained network is only specific to the studied system
Communication-Based	• Accurate • Can apply to coordination relays • Do not require any complex algorithm	• Delay due to the communication line • Lack of the standard protocols for the DC Microgrids • Need backup protection for the communication failures • Can be influenced by noise

Chapter 3

Local Fault Detection Scheme for DC Microgrids and Clusters

Based on JP5 and JP7, this chapter proposes local fault detection scheme for DC Microgrids and Clusters

3.1. Fault Characteristics in DC Systems

3.1.1. LIF Characteristics

As mentioned before, fault in DC Microgrids are categorized as LIFs and HIFs. LIFs are generally considered as the most serious and hazardous condition for power electronic converters. The equivalent circuit of DC/DC and AC/DC converters are presented in Fig. 2. During the fault, DC link capacitors start to discharge through the fault path, as a DC source. Therefore, the discharge current of these capacitors is exponentially decaying as (1). In addition, the current and voltage of the capacitors arecalculated by

$$V_C = \frac{V_0\omega_0}{\omega} e^{-\alpha t} \sin(\omega t + \beta) - \frac{I_0}{\omega C} e^{-\alpha t} \sin(\omega t) \quad (1)$$

$$I_{fault} = C\frac{dv_C}{dt} = -\frac{I_0\omega_0}{\omega} e^{-\alpha t} \sin(\omega t - \alpha) + \frac{V_0}{\omega L} e^{-\alpha t} \sin \omega t \quad (2)$$

$$t_1 = t_0 + (\pi - \lambda) / \omega \quad (3)$$

where

$$\begin{cases} \alpha = R_{dc} / 2L_{dc} \\ \omega = \sqrt{\dfrac{1}{L_{dc}C} - (\dfrac{R_{dc}}{2L_{dc}})^2} \\ \beta = \tan^{-1}(\dfrac{\omega}{\alpha}) \\ \lambda = \tan^{-1}(\dfrac{V_0\omega_0 C\sin\beta}{V_0\omega_0 C\cos\beta - I_0}) \end{cases} \tag{4}$$

where L_{dc} and R_{dc} are the inductance and resistance from converter location to the faulty point, respectively. t_0 is fault time, $I_{0,}$ and V_0 are normal current and voltage, respectively, and C is the capacitor of the converter. After the discharging of capacitors and reaching the voltage to zero, the fault current starts to flow through the diodes. Thus, the fault current at this stage can be obtained by

$$I_{fault} = I_0 e^{-(\frac{R_{dc}}{L_{dc}})t} \tag{5}$$

where I_0 is the initial value of fault current at the freewheeling diode stage. Since the magnitude and *di/dt* of LIFs are high, the diode could be damaged, therefore, the fault should be detected before reaching the voltage to zero. Consequently, it can be concluded that LIFs require fast fault detection methods. It could be noted that, due to the higher filter size of AC/DC converters, compared to DC/DC converters, the fault contribution of AC/DC converters is higher than DC/DC converters. Thus, under the condition of $R_{dc} < 2\sqrt{L_{dc} / C}$, the fault should be cleared quickly, and then a parameter is defined in this work to determine the maximum clearing time (MCT) of a fault detection method. The value of MCT is calculated by

$$MCT = t_1 - t_0 - t_O - t_d \tag{6}$$

where, t_d and t_o are the delay of measurements and operation time of SSCB, respectively. Therefore, to guarantee the safety of power electronic converters, the fault detection system should detect faults less than an MCT.

Fig.3 presents the different stages of fault in a DC system. The LIF has occurred at $t = 1$ s, and the first milliseconds are the capacitive discharge stage. After t_1, the freewheeling diode and decreasing current stage start.

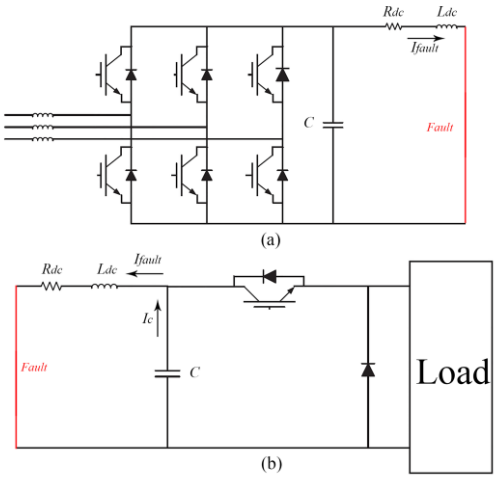

Fig. 2. Equivalent of (a) AC/DC (b) DC/DC converter during fault (Figure from JP5)

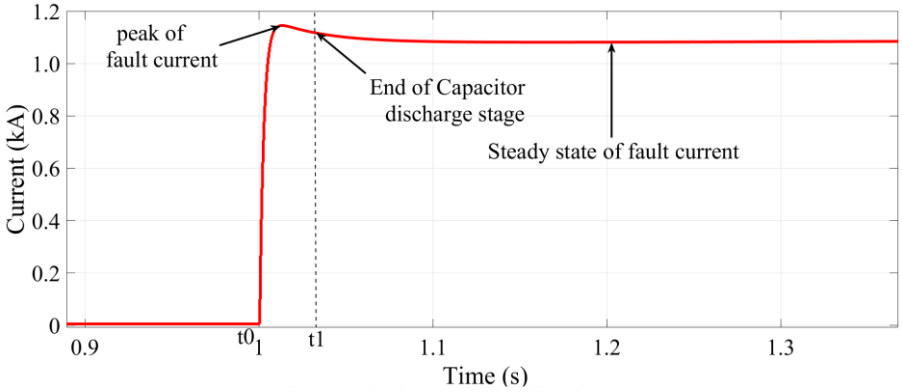

Fig. 3. Fault current in the DC Microgrid.(Figure from JP5)

3.1.2. HIF Characteristics

Since a conductor of DC cables connects to the ground or another cable by a high resistance surface, a HIF will happen. In HIFs, the fault current has a low magnitude, and then, the detection of this small change in current is one of the main problems of protection systems. If the protection system doesn't detect and isolate the HIF, it causes a repetitive reignition current [35]. Therefore, the first step of considering and designing a HIF protection function is modeling and realizing this concept. The characteristic of HIFs is divided into three parts, buildup, shoulder, and nonlinearity. At the buildup stage, the fault current increase to its maximum amplitude, then, the shoulder stage will start. The nonlinearity part defines the nonlinear characteristic of HIFs. In designing of HIF protection function, the accurate model of HIFs in DC Microgrids has been considered rarely. The performance of HIFs can be modeled by [36]

$$\begin{cases} i_{j+1} = i_j - \dfrac{Ri_j + k / i_j^{1.2} + 35 - V_{DC} \sin \omega t}{R - 1.2k / i_j^{2.2}} \\ 2n\pi + \pi / 3 < \omega t < 2n\pi + 2\pi / 3 \qquad n = 0,1,2,... \end{cases} \tag{7}$$

Therefore,

$$R = \frac{1.2ki_{j+1} / i_j^{2.2} - 1.2k / i_j^{2.2} - k / i_j^{1.2} - 35 + V_{DC} \sin \omega t}{i_{j+1}} \tag{8}$$

where k is the arc constant, i is the fault current, V_{DC} is the voltage rating, and R is equivalent resistance. The modeled HIF current is depicted in Fig. 4, which shows a repetitive current with a small magnitude. In the current work, this model is used during the designing of the HIF protection system.

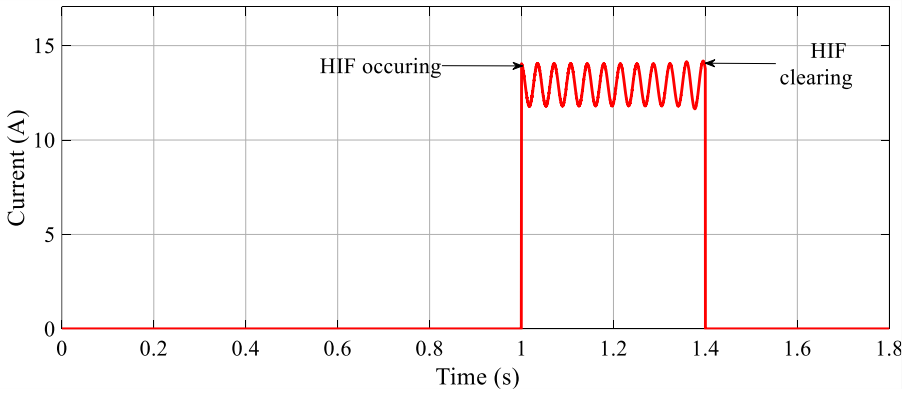

Fig. 4. Fault current of a HIF model (Figure from JP5).

3.2. DC Microgrid and cluster structure

The general structures of DC Microgrids and DC Microgrid clusters are presented briefly in this section. The general structure of a DC Microgrid can be represented as shown in Fig. 5. As shown in Fig. 5, the fault current is made by the sum of currents of all RESs and grid. Despite the unidirectional fault current in radial systems, the fault current is fed by bidirectional currents. Thus, it causes complexity in the protection of mesh DC Microgrids.

The installation location of protection relays depends on the type of protection system in terms of using or lack of communication link. Therefore, due to the localized structure of fault detection and location in this work, the structure of relays in DC Microgrids is shown as Fig. 5.

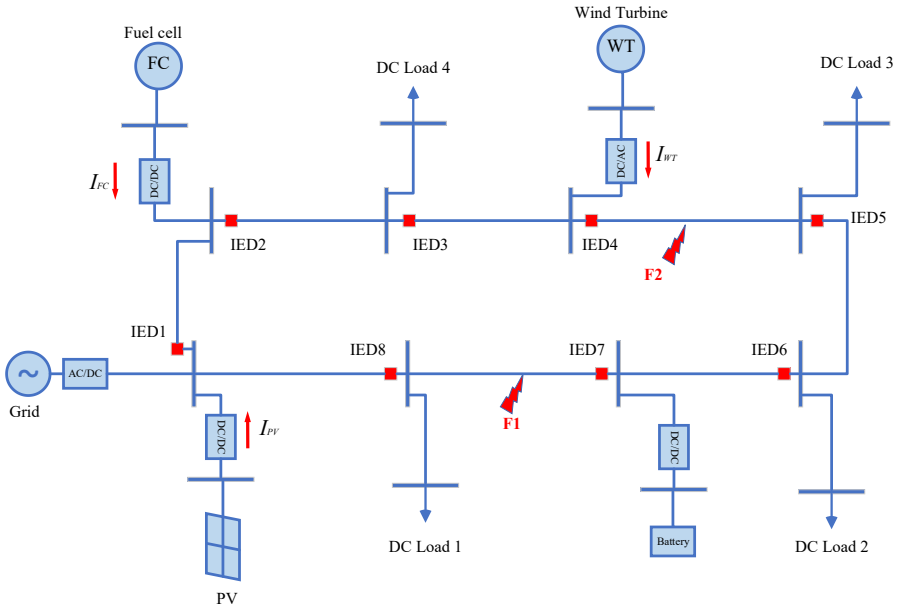

Fig. 5. The structure of a DC Microgrid

On the other hand, the structure of DC Microgrid clusters is shown in Fig. 6. In these systems, several DC Microgrids are connected together to provide more power support capability. However, the high penetration of RESs and the transmission line between DC Microgrids increase the difficulty of the protection of these systems. In local protection systems, the relays are implemented on both sides of each line without any communication links. In clusters, due to the power-sharing between DC Microgrids, there is no guarantee on the direction of current during normal conditions; therefore, the protection devices should be equipped by directional methods.

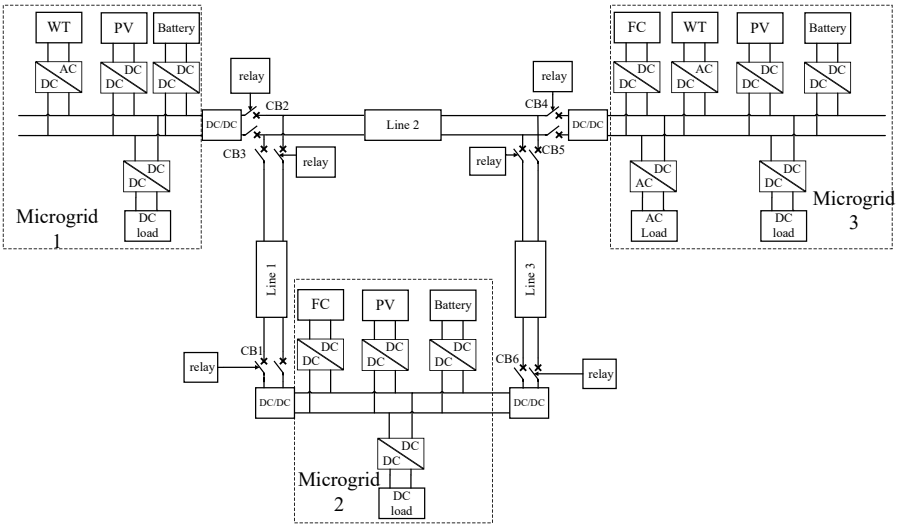

Fig. 6. The structure of a DC Microgrid cluster (Figure from JP7).

3.3. Proposed Mathematical Morphology-based Fault Fetection Method

3.3.1. Basic of Mathematical Morphology

Mathematical Morphology (MM) is introduced in [37] as a time-domain signal processing tool. Despite the other signal processing tools, such as Fourier transform and wavelet, the MM is a non-periodic tool. Moreover, MM is a straightforward and fast operator without using any multiplication and division operations. In DC systems, the frequency-domain signal processing tools have lower suitability than time-domain tools, due to the non-periodic characteristic of fault current.

MM is based on two transformations, dilation, and erosion. The dilation and erosion are considered as swelling and shrinking procedures, respectively as

$$y_D(n) = (f \oplus g)(n) = \min(f(n-m) + g(m)) \quad 0 \le (n-m) \le N, m \ge 0 \tag{9}$$

$$y_E(n) = (f \ominus g)(n) = \min\big(f(n+m) - g(m)\big) \quad 0 \le (n+m) \le N, m \ge 0 \tag{10}$$

where *g(m)* is the structural element (SE), *f(n)* is the original signal, and *N* is the total number of samples. SE is the base of MM, and it is a probe for feature extraction of the original signal [38]. The shape, height, and length of the SE impact on the MM results. Thus, the selection of SE should be chosen based on the application of MM. Based on the dilation and erosion, the foundation of the MM filter is calculated by (10). The closing and opening performance of the MM filter refers to the narrowing valleys and sharping edge, respectively. The closing and opening filters are obtained by

$$y_C(n) = (f \cdot g)(n) = ((f \oplus g) \ominus g)(n) \tag{11}$$

$$y_O(n) = (f \circ g)(n) = ((f \ominus g) \oplus g)(n) \tag{12}$$

where y_C and y_O are the outputs of the closing and opening filters, respectively.

3.3.2. MM Regional Maxima

The MM regional maxima sends the signals to the fault detection device for comparing them with a threshold. The value of the threshold is defined as the border between faults, HIF, and overload conditions. Thus, the values of the threshold are selected based on a 20% overload. During the first stage of fault, the fault current reaches its peak. Therefore, the value of MM regional maxima starts to increase faster the original signal. The MM regional maxima have all samples higher than any current amplitude in its finite numbers of neighborhoods. They obtained from the residue of the h-maxima of height 1. The h-maxima transform tool represses any domes with a high equal or smaller than the threshold value and reduces the height of the other domes by a threshold value. It is determined the reconstruction by dilation of *f* subtracted

by the height of the threshold value. Therefore, it detects the fault within peak time, which guarantees the safety of power electronic converters.

3.3.3. DC Fault Current Detection

The MM-based filter extracts the transient features of the fault current and removes the noise from the main measured signal. The output of the filter will be the input of the MM regional maxima. As shown in Fig. 7, the fault detection detects faults immediately within the peak time. Consequently, the proposed method ensures the safety of power electronic converters. Also, by using SSCBs, the operation time of the isolation will be low, and due to the lack of communication channels, the delay in this method is avoided.

As shown in Fig. 7, the MM regional maxima increases to a high value faster than the original fault current signal, and it sends directly to the SSCBs for isolation of the faulty section. By using the erosion filer, this scheme is invulnerable to the noise. Fig. 8 represents the diagram of the proposed method for fault detection on DC Microgrids and DC Microgrid clusters. This method only needs the current signal of one end of a line segment, then, the requiring of the communication infrastructure is eliminated between measurement devices of both ends of the line.

Another important and essential function of fault detection schemes is selectivity, which refers to that the SSCBs only trip during fault at their protection zone. Therefore, in this work, an additional parameter is added to the operation time of each fault detection system. The fault current magnitude will decrease by increasing the distance from the faulty point. Thus, the closer sensors to fault measure a higher magnitude, and the closer protection system should operate faster than other devices. Therefore, the operation time of each protection device is obtained and sent to SSCBs by

$$t = t_D + \frac{\xi\psi}{I_D} \tag{13}$$

where ξ and ψ are MM signal magnitude and the constant value, respectively, I_D is the fault current at detection moment, t_D is the primary detection time. In this work, ψ is assumed 10000. The range of $\xi\psi/I_D$ is around several microseconds. Then, it cannot cause a significant delay in SSCB operation times, but, it provides a suitable selectivity for the proposed protection scheme.

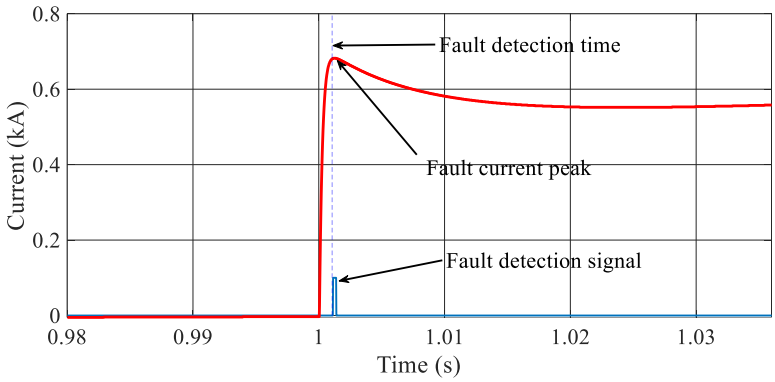

Fig. 7. MM regional maxima of fault current in DC Microgrid cluster (Figure from JP5).

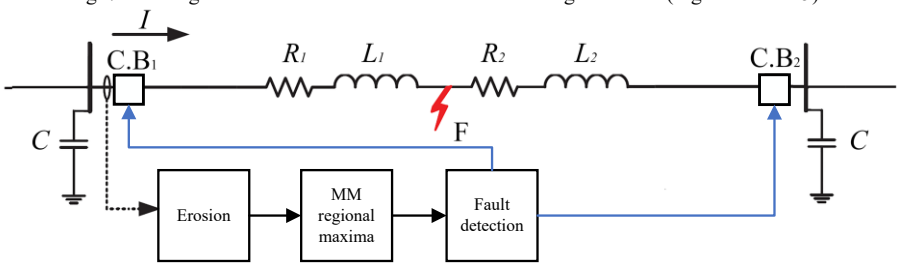

Fig. 8. Diagram of the proposed fault detection scheme (Figure from JP5).

3.3.4. HIF Fault Detection

As mentioned before, the important and challenging types of faults to detect is HIFs. As shown in Fig. 4, the HIF current is spiky and repetitive. Fig. 9 shows the operation of the proposed scheme during a HIF. Based on (8), the

fault current has a small change during HIFs and based on Fig. 8, the fault is detected immediately. Thus, this method does not need any function for distinguishing LIFs and HIFs.

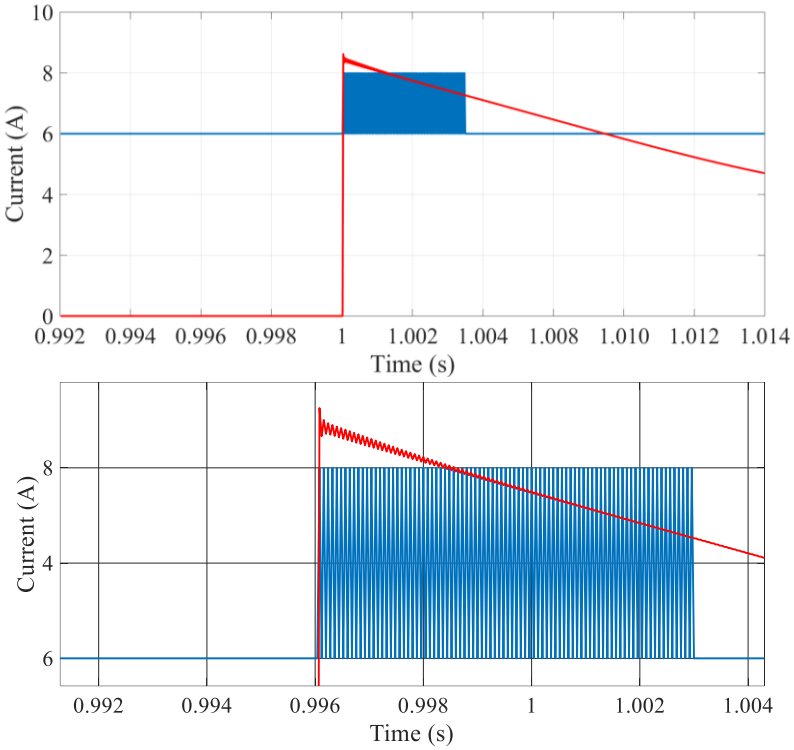

Fig. 9. Fault current and the fault detection signal during HIF (Figure from JP5).

3.3.5. Experimental Results of MM-based Fault Detection Method

Different experimental tests are applied to the scaled setup consists of dSPACE, equivalent line segment, converters, and power supplies, as represented in Fig. 10. In this work, HIFs and LIFs are occurred in different locations with different fault resistances and measured by a current sensor at only one end of the line with a sampling rate of 50 kHz.

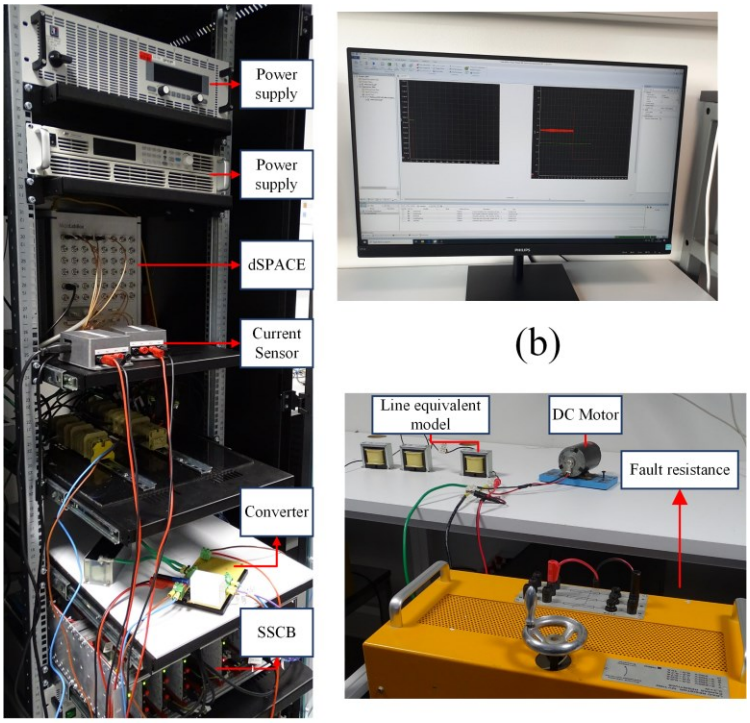

Fig. 10. The experimental test setup (a) power supplies, dSPACE, sensors, converter, SSCB, (b) dSPACE interface, (c) loads, line, fault resistance (Figure from JP5).

A LIF by fault resistance of 3.2 Ω has occurred at 30% of the line, and the current is shown in Fig. 11. The MM-based fault detection function is designed in the dSPACE, and, within 2.18 ms, the fault is detected, as shown in Fig. 12.

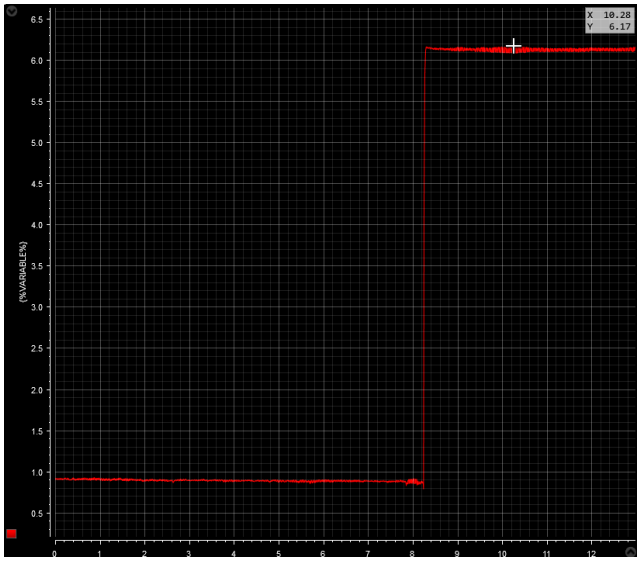

Fig. 11. The fault current waveform of a LIF (Figure from JP5).

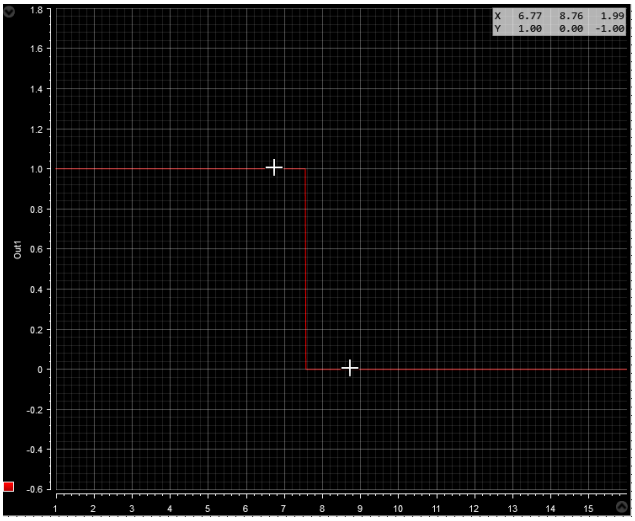

Fig. 12. The fault detection signal during LIF (Figure from JP5).

Based on Fig. 12, and 13 LIF is detected within peak time and ensures the safety of the power electronic converters. On the other hand, the effectivity of the proposed scheme in the case of HIFs is investigated as shown in Fig. 14, which a HIF with fault resistance of 50 Ω applied to the system. Then the tripping signal is sent to SSCBs within 3.8 ms. The fault detection results of

this work during both HIFs and LIFs proves an extremely low operation time to avoid any damages to converters.

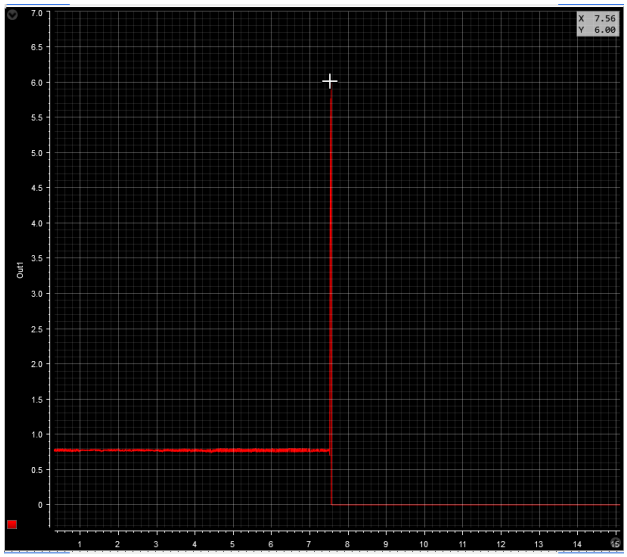

Fig. 13. The fault current waveform of LIF after (Figure from JP5).

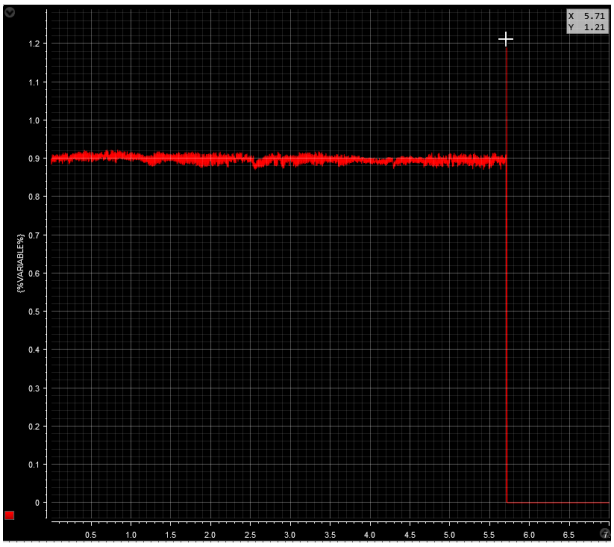

Fig. 14. The fault current isolation during a HIF (Figure from JP5).

3.4. Empirical Mode Decomposition (EMD) based Fault Detection Method

3.4.1. EMD

As shown in Fig. 15, a transient signal is made by its oscillation modes, and inherent features are retrieved from non-sinusoidal signals by calculating the higher and lower envelopes of it.

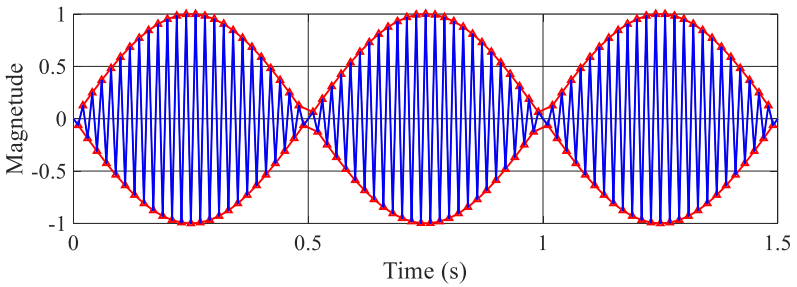

Fig. 15. Depicting the configuration of a lower and upper envelope of a signal (Figure from JP7).

Then, the average of both lower and higher envelopes are used to determine a mean oscillation signal. This signal is the first oscillation component, intrinsic mode function (IMF), estimation. The second component is obtained by subtraction the first component and the original signal. These explanations present the EMD principles [39]. Consequently, by using EMD, any non-sinusoidal transient signal can be divided into several fluctuating components. Another principle of EMD is that the integral of IMF should be zero and the numbers of extremums and zero-crossing points should be equal. The steps of EMD for fault detection are presented as follows

1. Determine the local minimums and extremums, and find the higher and bottom envelopes.
2. Obtain the envelope mean value (m_1). Calculate the h_1 by the difference between the m_1 and original signal as

$$x(t) - m_1 = h_1 \tag{14}$$

3. Repeat steps 1 to 3 with h_1 to calculate h_{11}, where is an inherent mode function as

$$h_1 - m_{11} = h_{11} \tag{15}$$

4. If h_{11} satisfies the conditions of IMF, then the first IMF is determined, else the steps should be repeated, and after n times the h_{1n} will be

$$h_{1(n-1)} - m_{1n} = h_{1n} \tag{16}$$

5. The first IMF is h_{1n}, then

$$r_1 = x(t) - h_{1n} \tag{17}$$

6. Where, the original signal is r_1, and steps 1 to 5 should be repeated to calculate the second IMF.

7. Repeat steps 1 to 6 to determine all the IMFs of the original signal.

In this proposed scheme, the EMD is utilized for fault detection in DC Microgrid clusters. For providing an online EMD, the input signal is a time-dependent function, and the statics are defined as

$$s(t_1), s(t_2), ..., s(t_m) \tag{18}$$

where $s(t_1)$ to $s(t_m)$ is the primary to mth sectioned points. For storing data, different windows are considered, and each window has a length of l as

$$\begin{aligned} &\text{section1}: s(t_1), s(t_2), ..., s(t_l) \\ &\text{section2}: s(t_{l+1}), s(t_{l+2}), ..., s(t_{2l}) \end{aligned} \tag{19}$$

3.4.2. Hilbert-Huang transform (HHT)

In the proposed fault detection method, after calculating IMFs, the HHT is applied to determine the instantaneous frequency and magnitude. The HHT values, $H_i(t)$, for each time signal ,$c_i(\sigma)$, is calculated by

$$H_i(t) = \frac{1}{\pi} P \int_{-\infty}^{\infty} \frac{c_i(\sigma)}{t-\sigma} d\sigma \tag{20}$$

where P is the value of the singular integral principal, and typically is 1. This is used to obtain an analytical signal, z(t) as

$$z_i(t) = c_i(t) + j d_i(t) = a_i(t) e^{j\varphi_i(t)} \tag{21}$$

where

$$\begin{cases} a_i(t) = \sqrt{c_i^2(t) + d_i^2(t)} \\ \varphi_i(t) = \arctan(\dfrac{d_i(t)}{c_i(t)}) \end{cases} \tag{22}$$

Then, the frequency will be

$$\omega_i(t) = \frac{d\varphi_i(t)}{dt} \tag{23}$$

Thus, the instantaneous frequency signal is determined by

$$hht(t) = \mathrm{Re} \sum_{i=1}^{m} a_i(t) e^{j\int \omega_i(t) dt} \tag{24}$$

where *hht(t)* is the Hilbert amplitude, and Re is the real part. Eq. (24) presents the signal based on the instantaneous magnitude and frequency. Also, it presents that the original signal can be defined by sum of the IMFs and the HHT magnitudes. Moreover, the HHT has significant results on mono-component signals, but, the signals of majority practical applications are noisy multi-components. Thus, the HHT will provide spurious magnitude at negative frequency. To solve it, in EMD-HHT methods, due to the analysis of a series of IMFs, signals do not have any noises.

The proposed fault detection method uses a hybrid EMD-HHT method on DC Microgrid clusters. The EMD helps to avoid noise and extracting fault

current features, and HHT detects the LIFs and HIFs by IMFs and it will minimize the impact of fault resistance. In the first step, the sensor measures the fault current at SSCB places. Then, the fault current is analyzed by the proposed method to detect the fault. In normal conditions, the output of the relay is zero, but, during the fault, the first IMF is observed and the HHT determines the magnitude and frequencies. Due to the frequency-based nature of the proposed scheme, this approach immune to changing the fault resistance. Thus, the HIF with a high value of fault resistance and low fault current magnitude will be detectable. The steps of the proposed method are as follows

Step 1: Sensors measuring the current.

Step 2: Determining the first IMF by EMD, and investigating it by HHT of fault detection relay.

Step 3: During the conditions with output value lower than a threshold, ϵ, the operation mode of systems categorized as normal mode, else, the fault mode.

Step 4: Send the trip signal to the SSCBs.

The value of the threshold is calculated based on the worse case of overload, which is normally selected for 120% overload.

3.4.3. Simulation Results of EMD-based Fault Detection Method

In the simulation environment, a LIF at the interconnection link at t = 0.3 s with fault resistance of 0.01 Ω has occurred. The HHT, IMF, and fault current signals are shown in Fig. 16. The peak time of the fault current is 20 ms, and the detection time is 0.6 ms. On the other hand, a HIF has occurred at t = 0.3 s with fault resistance of 20 Ω, and signals are shown in Fig. 17, and

the fault is detected within 2.2 ms. The high speed of fault detection proves the effectivity of the proposed method, and it guarantees the safety of power electronic converters.

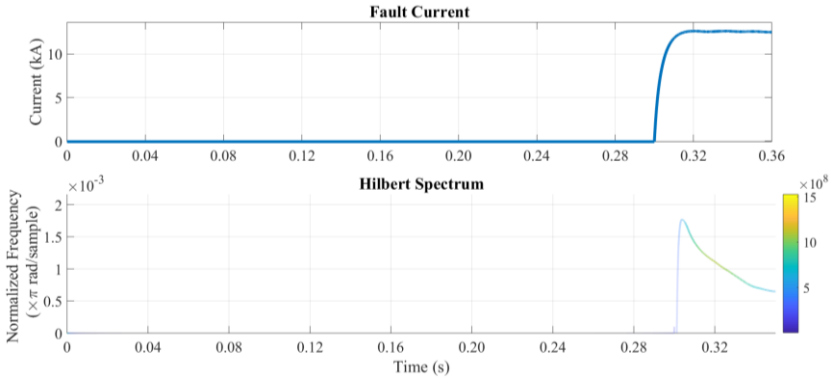

Fig. 16. Fault current and detection signals for a fault at interconnected link 1 with fault resistance of 0.01 Ω at $t = 0.3$ s (Figure from JP7).

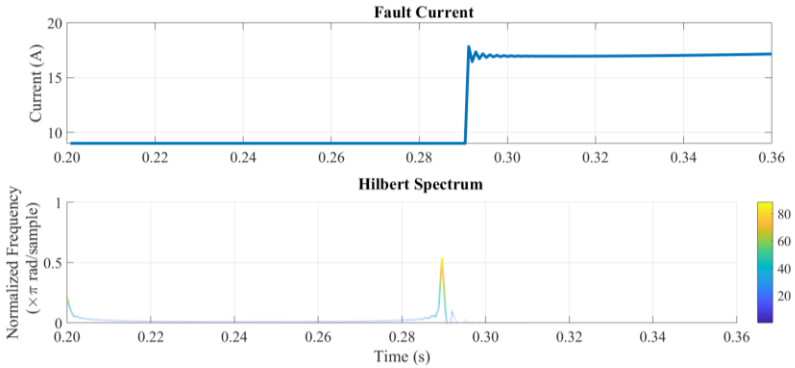

Fig. 17. Fault current and detection signals for a fault at interconnected link 3 with fault resistance of 20 Ω at $t = 0.3$ s (Figure from JP7).

The performance of the proposed scheme in noisy conditions with bad calibration under overload is shown in Fig. 18. In this scenario, noise causes 2%, and bad calibration is modeled by 1% variation in fault current values. Moreover, a 10% overload is immediately connected. The fault detection signal proves the significant operation of the proposed scheme under different disturbances and the fault detection relay has not been sent the trip signal to the DC C.Bs.

In addition, Table 2 and Table 3 show the performance of the proposed method under different scenarios such as the investigation of the bad calibration and noise. The comparing between Tables 2 and 3 shows a slight impact of noise only on the detection time of HIFs. Although bad calibration has a higher influence on both HIFs and LIFs, the fault detection time of the proposed scheme remains in an appropriate range.

Table 2. Table from JP7, fault detection time for different fault conditions

Fault location	**Fault resistance**	**Detection time**	**Fault location**	**Fault resistance**	**Detection time**
Line 1	0.01 Ω	0.6 ms	Line 3	0.8 Ω	0.8 ms
Line 1	0.4 Ω	0.7 ms	Line 3	1.7 Ω	0.9 ms
Line 1	3.7 Ω	1.1 ms	Line 3	7.5 Ω	1.3 ms
Line 1	10 Ω	1.7 ms	Line 3	20 Ω	2.2 ms
Line 2	0.05 Ω	0.6 ms	DCMG1	0.2 Ω	0.6 ms
Line 2	0.5 Ω	0.7 ms	DCMG1	2 Ω	1.0 ms
Line 2	5 Ω	1.2 ms	DCMG2	2.5 Ω	1.1 ms
Line 2	15 Ω	1.9 ms	DCMG3	2 Ω	1.0 ms

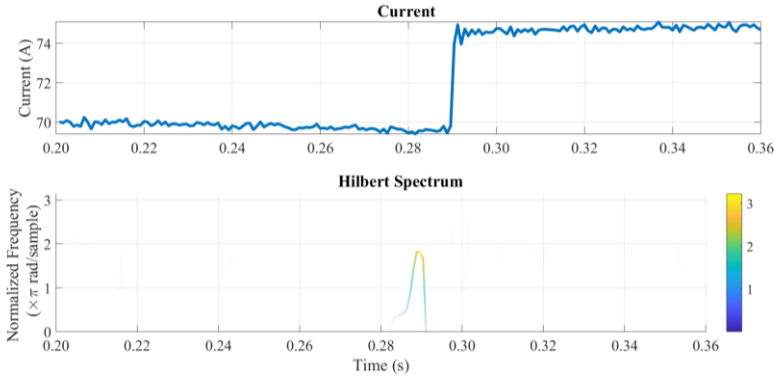

Fig. 18. Current and detection signals under overload, noise and bad calibration (Figure from JP5).

Table 3. Table from JP7, fault detection time for noise, bad calibration

Noise			Bad calibration		
Fault location	**Fault resistance**	**Detection time**	**Fault location**	**Fault resistance**	**Detection time**
Line 1	0.01 Ω	0.6 ms	Line 1	0.01 Ω	0.7 ms
Line 1	0.4 Ω	0.7 ms	Line 1	0.4 Ω	0.9 ms
Line 2	0.05 Ω	0.6 ms	Line 2	0.05 Ω	0.6 ms
Line 2	5 Ω	0.8 ms	Line 2	5 Ω	1.6 ms
Line 3	7.5 Ω	1.3 ms	Line 3	7.5 Ω	1.9 ms
Line 3	20 Ω	2.3 ms	Line 3	20 Ω	2.8 ms

3.5. Fuse Saving Method

In DC Microgrids, the fault current causes a bidirectional flow with different fault current levels, and therefore, it may result in miscoordination of DC fuses and reclosers. In this section, a fuse saving technique by finding the appropriate settings of DC fuses and the recloser switch is proposed. The proposed protection scheme is localized, and it is applicable for digital and conventional protection devices.

Despite the unidirectional current flow in radial systems, the fault current is made by different current flows to provide a bidirectional current. Thus, the

fault current from the grid side affects all lines of the system, and using a recloser switch at the connection point of the grid and DC Microgrids can control the fault current during the temporary faults to save fuses. Moreover, all RESs of the system contribute to the fault current from both sides of the faulty point, thus, it increases the complexity of the coordination of recloser switch and DC fuses.

In selecting DC fuses, finding the operation time of these devices is the challenging part. The fault current rise is based on *L/R*, the time constant, thus, the inductance of system and arc have significant differences. In AC systems, the melting time is from 4 ms to a few cycles, however, in DC Microgrids, since the fault current needs more time to reach the steady-state condition, the DC fuses take more time to melt. For instance, in a DC system with *L/R* lower than 10 ms, the DC fuse has the same operation curve with AC fuses, however at the higher current portion, it has a small difference. For *L/R* higher than 10 ms, the isolation time of the fault by fuses is slow, since the slow increase in the fault current. The impact of *L/R* on the operation of DC and AC fuses is shown in Fig. 19.

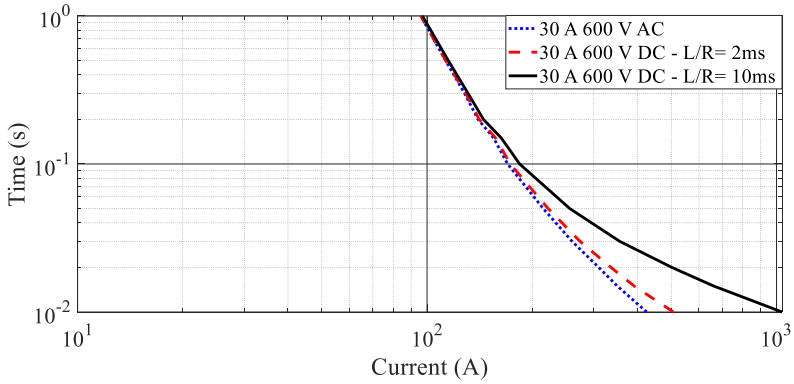

Fig. 19. The *L/R* impact of fuses (Figure from JP3).

Based on Fig. 19, only DC fuses for situations with the low value of *L/R* can use the characteristic curve of AC fuses. However, based on the differenced of AC and DC fuses, the characteristic curve of DC fuses should

be defined in terms of *L/R*. During fault in DC Microgrids, the DC line is equivalented by the inductance-resistance circuit. Thus, the fault current is defined by:

$$I_i = I_f(1 - e^{-n}) \tag{25}$$

where I_i is the instantaneous current, n is the number of the time constants, and I_f is fault current, and it is determined by the initial value of voltage, V, and resistance, then I_f is V/R. On the other hand, the DC fuses heating effect during melting is obtained by the RMS value of (25) as follows:

$$I_{rms} = (\frac{1}{T}\int_0^T i^2(t)dt)^{0.5} \tag{26}$$

where T is the period over which integrated. By substituting of (25) into (26), the I_{rms} is calculated by:

$$I_{rms} = I_f(1 + 2\frac{e^{-n}}{n} - \frac{e^{-2n}}{2n} - \frac{1.5}{n})^{0.5} \tag{27}$$

Moreover, the value of n is tR/L. And, the characteristic curve of AC fuses obtained by:

$$\log(t_{fuse}) = a\log(I_f) + b \tag{28}$$

where a and b are the settings of fuse, and t_{fuse} is the operation time of fuse. Based on (27), the characteristic curve of DC fuses is calculated by

$$\log(t_{fuse}) = a\log(\frac{I_f}{(1 + 2L\frac{e^{-tR/L}}{tR} - L\frac{e^{-2tR/L}}{2tR} - L\frac{1.5}{tR})^{0.5}}) + b \tag{29}$$

Therefore, (29) is the characteristic curve of the DC fuses. It represents that the high values of time constants have more differences in values of AC and DC fuse currents, especially in lower times.

Different types of protection devices such as relays, SSCBs, fuses, and recloser switches are implemented in the DC Microgrids. The primary

objective of a protection system is clearing both temporary and permanent faults within the lowest possible time and de-energizing the minimum zones of the system. Typically, the majority of faults are temporary and made by transient contacting of lines together or to ground. The temporary faults are cleared after several milliseconds to seconds. Moreover, the fast operation of the recloser switch should be ensured to avoid the unnecessary melting of DC fuses, and therefore, it saves the fuses and other maintenance costs.

Furthermore, the recloser switches and fuses have the characteristic curve of Fig. 20. Moreover, by increasing the maximum of fault current by installing RESs, from $I_{F,max}$ to I_1, the coordination between recloser switch and DC fuses will be eliminated. Also, due to the slow operation of the traditional reclosers, they cannot be used in the DC Microgrids to save fuses. Thus, downstream fuses should be coordinated by the operation of a recloser switch. Therefore, the operation curve of the recloser switch for permanent and temporary faults should be located in the upper and lower area of the fuse curve, respectively.

It should be noted that DC fuse clearing and melting I^2t values should be compared for assessing the selectivity of fuses. The I^2t value of downstream DC fuses should be less than the melting I^2t value of upstream DC fuses.

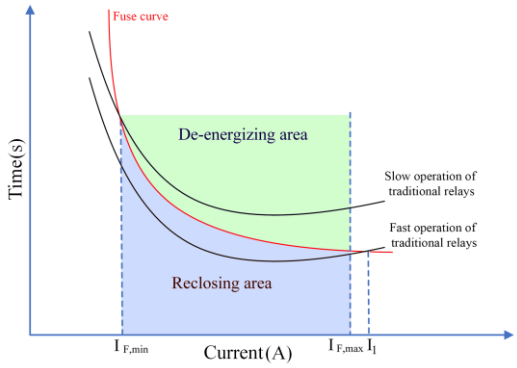

Fig. 20. The characteristic curve of fuse (Figure from JP3).

3.5.1. Proposed Protection Strategy and Coordination for Recloser Switch and Fuse

During fault in DC Microgrids, the IGBTs of converters are blocked and leaves the diodes exposed to the fault current. However, the fault current tolerant of diodes is high, and the thermal limit of diodes determines by I^2t, should be considered during the selection of fuses. Then, the converter capacitors discharge through the line faulty path.

During the capacitor discharge stage, as represented in (2), the fault current is depicted in Fig. 21. Then, the maximum value of fault current occurs at

$$t_{\max} = \frac{1}{\omega}\tan^{-1}\left(\frac{2\alpha\omega I_0 - \omega V_0/L}{\alpha^2 I_0 - I_0\omega^2 - \alpha V_0/L}\right) \tag{30}$$

where t_{max} is the time of peak time. Also, the value of fault current cannot exceed the I^2t of components. Thus, a current factor for the setting of recloser switches is determined by

$$I_{Setting} = \sigma - I_{F,\max} \tag{31}$$

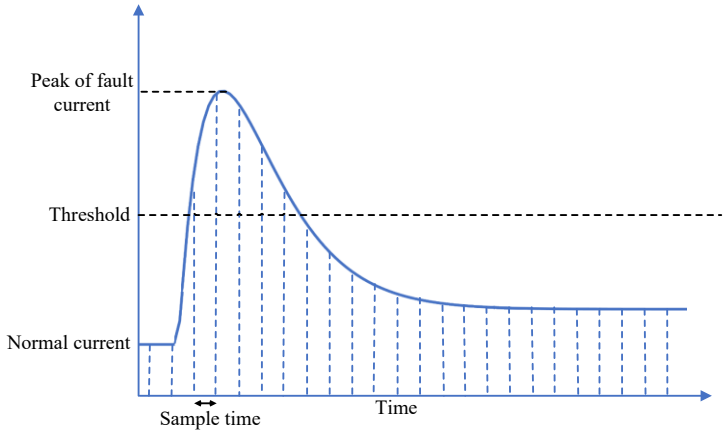

Fig. 21. The fault current behavior of the DC circuit (Figure from JP3).

where σ is the short term thermal tolerant, and $I_{Setting}$ is the setting of recloser switch. Thus, (31) and (32) are setting the recloser switch. Consequently, the

recloser switch uses the t_{max} and $I_{Setting}$ for setting parameters, and the *I-t* curve as an inverse time-current curve, as shown in Fig. 22. The fast and slow operation curves isolate during temporary and permanent faults, respectively, and they are located below and upper the fuse characteristic curve, respectively. The proposed *I-t* curve is shown in Fig. 22. In addition, the general equation of the recloser switch is indicated in

$$t_{\max} = Ae^{-BI_{settings}} + Ce^{-DI_{settings}} \tag{32}$$

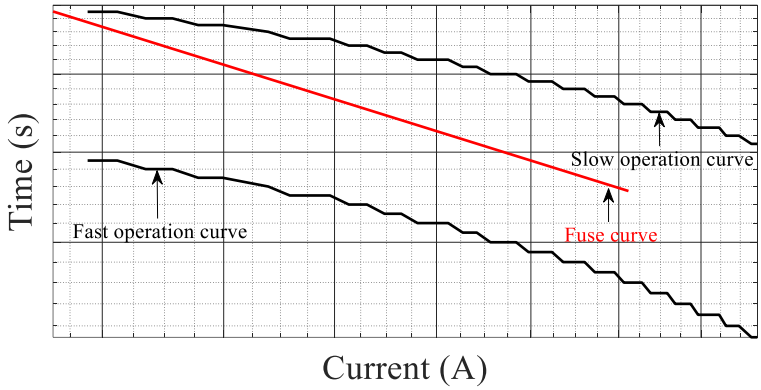

Fig. 22. Inverse time-current characteristic curve of the proposed recloser switch (Figure from JP3).

where *A*, *B, C,* and *D* are the settings of the recloser. In addition, since the fuse and recloser switch curves have exponential nature, these curves can be presented in logarithmic figures. After detecting a temporary fault, the recloser switch isolates the power line, then by specific delay, after clearing the fault, the system will back to the normal conditions; however, during the permanent faults, if the fault remains in the system, recloser switch trips again. The flowchart of the proposed technique is presented in Fig. 23. Thus, the proposed method clears both permanent and temporary faults by the lowest operation time and saves the fuses during temporary faults.

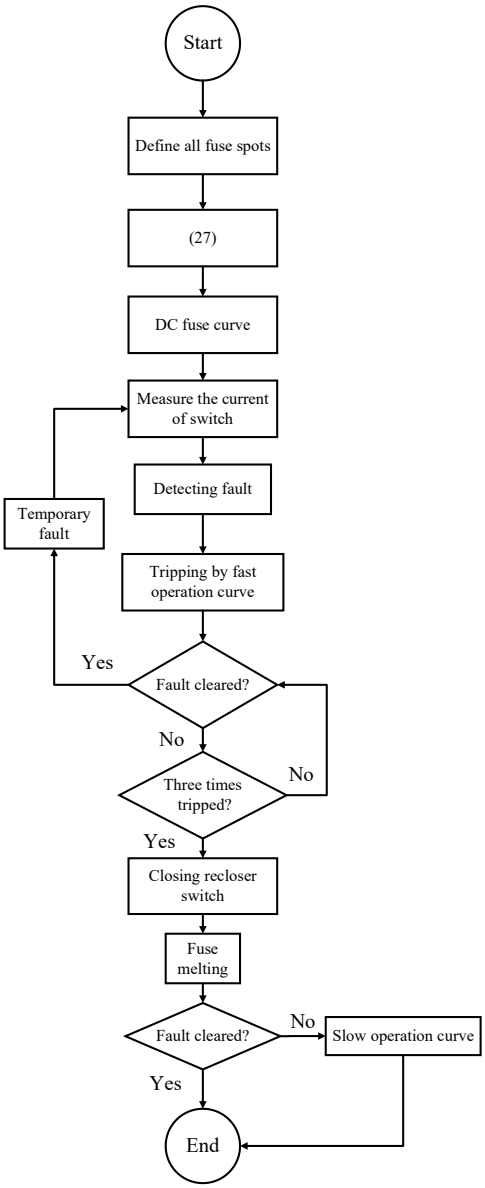

Fig. 23. The flowchart of the proposed method (Figure from JP3).

3.5.2. Results of the Proposed Fuse Saving Method

The effectiveness of the proposed technique is validated by simulations on a DC Microgrid, as shown in Fig. 24. A DC Microgrid is suggested for

implementation in Rømø island in Denmark consists of PV, fuel cell (FC), battery, WT, and loads, as the grid-connected mode by an AC/DC converter. The protection system of the suggested island DC Microgrid is consisting of DC fuses, and recloser switch.

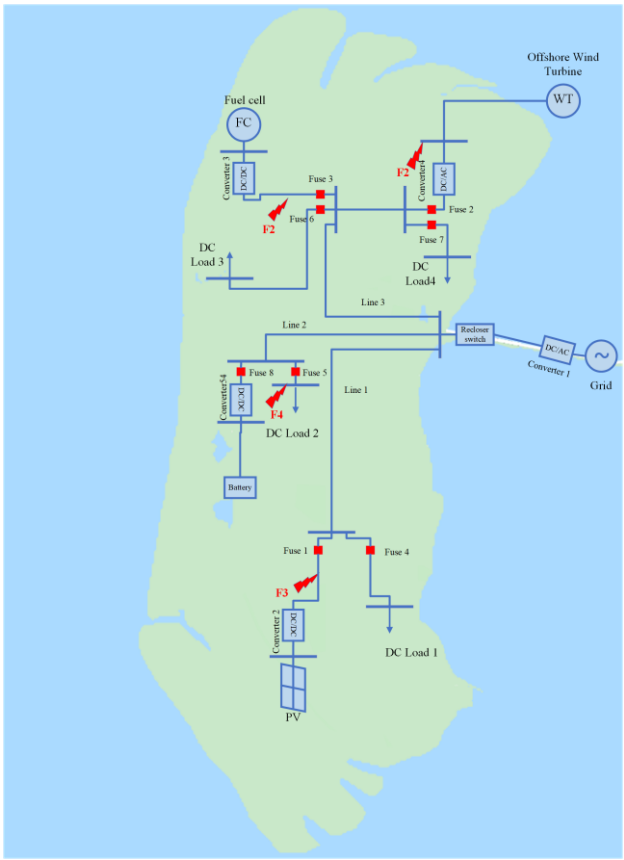

Fig. 24. The Rømø island DC Microgrid case study (Figure from JP3).

First, the peak value and time of fault for different locations and fault resistances are defined for determining the fast operation curve of the recloser switch. To obtain the settings of the recloser switch, faults are simulated at all locations with different fault resistances. The data of the fault current peak for different situations generates the operation curve of the recloser switch.

In the second step, the performance of the recloser switch is calculated, and, the values of the recloser setting are depicted as Fig. 25, and the parameters of estimation are shown. This curve presents that increasing the fault current decreases the operation time of the recloser switch. Consequently, the characteristic curve of recloser is determined by

$$t_{\max} = 84.96e^{-0.09689 I_{settings}} + 0.09308e^{-0.0003729 I_{settings}} \tag{33}$$

The *I-t* curve of the recloser switch is depicted in Fig. 26. Then, the fuse operation curves are calculated by curve fitting, and the curve fitting is performed by using an optimization algorithm to find the best values of settings. Thus, the DC fuse curve of load fuses are defined by

$$\log(t_{fuse}) = -0.95\log\left(\frac{I_f}{(1+2L\frac{e^{-tR/L}}{tR} - L\frac{e^{-2tR/L}}{2tR} - L\frac{1.5}{tR})^{0.5}}\right) + 4.8 \tag{34}$$

Moreover, the value of *L/R* of loads in this work is assumed to be 2 ms. The fuse operation curves of fuses 1 to 8 are depicted in Fig. 26. In Fig. 26 (a), the time-current curve of DC fuses number 4 to 7, as load fuses are depicted, therefore, due to the same behavior of these loads, they have similar characteristic curves, and they are located between the fast and slow operation curves. On the other hand, other resources DC fuses have a different time-current curve, as shown in Fig. 26 (b). In these curves, DC fuse 1 has the highest operation curve, and DC fuse 2 has the lowest one. The reason for this has a different fault current magnitudes. The difference between the settings of fuses is due to the difference between the maximum value of the fault current of the protected branch by the corresponding fuse. For the case of increasing the value of fault current, due to the approximately fixed margin between fuse and recloser switch curves, it cannot jeopardize the operation of recloser switches in higher fault currents.

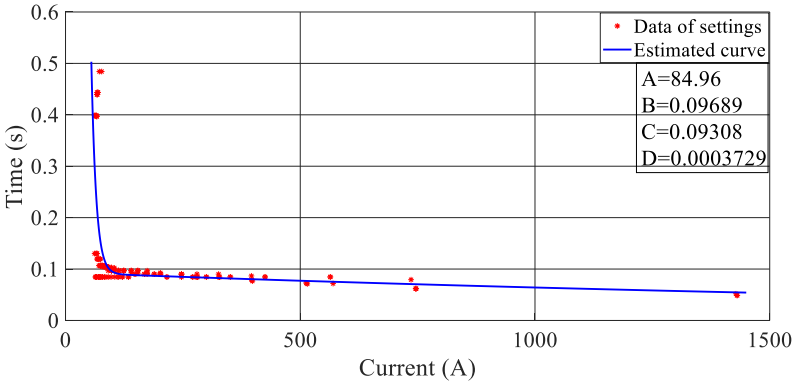

Fig. 25. The estimation of the recloser switch settings (Figure from JP3).

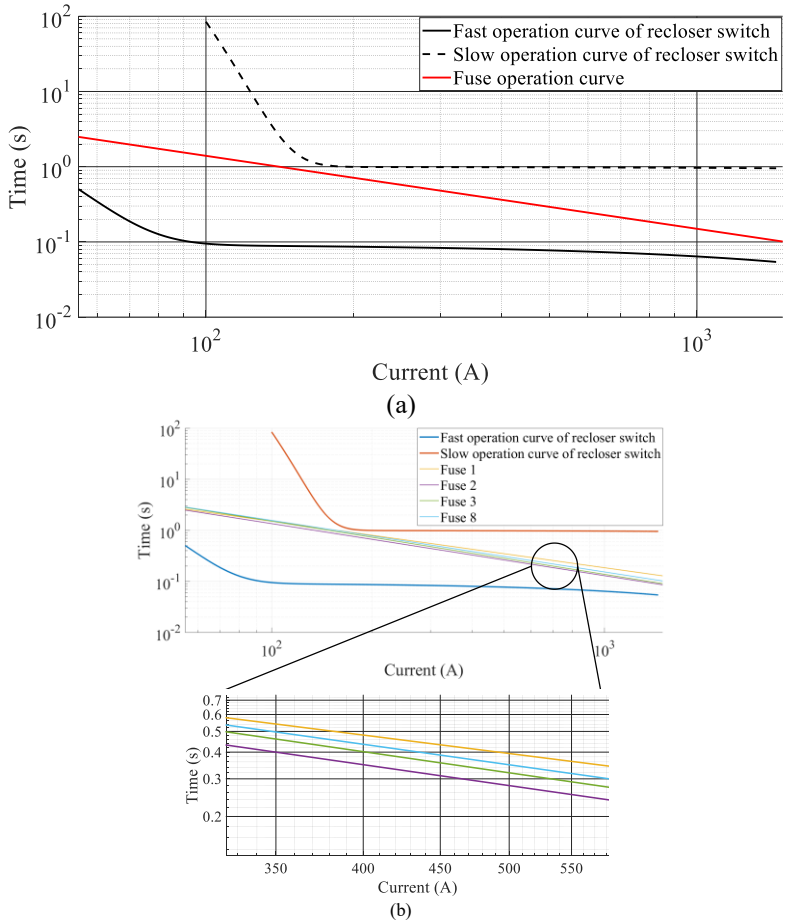

Fig. 26. The operation curve of (a) load fuses (b) resource fuses (Figure from JP3).

3.6. Comparison of Proposed Fault Detection Methods

The proposed methods are compared with [40]-[44] in terms of requiring communication facilities, the ability to detect HIFs, and fault detection time in Table 4. In [40], the differential fault detection method is used to detect faults in DC systems, however, it requires communication links, and a limited value of fault resistance is considered. [41] is a local fault detection method, however, the HIFs are not considered on it. In [42], HIF detection has not been considered and, this method does not need communication links. In [43], An intelligent three tie switch is suggested to detects HIF. But, the fault detection time is too high and it requires a communication link. [44] presents a wavelet-based HIF detection method without requiring any communication channels; however, it only applies only to radial DC systems.

The proposed MM and EMD based fault detection methods have 4 ms and 2 ms fault detection time, respectively, which both of them are in an acceptable range. Moreover, both of these methods can detect HIFs locally. Therefore, only in terms of fault detection, the EMD-based fault detection method has better performance than an MM-based fault detection scheme.

Table 4. Table from JP7, comparing of proposed method with existed methods

Method	Communication link	Cost	Detection time	HIF	Fault resistance	Sampling rate
[26]	Yes	High	110 ms	No	2 Ω	5 kHz
[27]	No	Moderate	20 ms	No	0 Ω	20 kHz
[28]	No	Low	4 ms	No	8 Ω	10 kHz
[29]	Yes	High	300 ms	Yes	20 Ω	--
[30]	No	Low	5.5 ms	Yes	300 Ω	--
MM-based Proposed method	No	Low	4 ms	Yes	50 Ω	50 kHz
EMD-based Proposed method	No	Low	2 ms	Yes	20 Ω	50 kHz

Chapter 4

Local Fault Location Scheme for DC Microgrids and Clusters

Based on JP2, JP4, and JP6, this chapter proposes local fault location schemes for DC Microgrids and Clusters

4.1. Fault Location Method of CPLs in DC Microgrids

In this section, the proposed fault location method for CPLs in a DC Microgrid is presented. The proposed method calculates the fault location and resistance only by one relay, and it obtains the fault resistance values by power-sharing and transient values of current and voltage at relay place without using any communication links.

4.1.1. The Behavior of CPLs During Fault

In DC Microgrids, the majority of loads are controlled and have a CPL performance. Due to the constant power, the connection between voltage and current is

$$P = V * I = \text{constant} \tag{35}$$

During a fault, (25) describe that the voltage drop causes a higher current increasing in CPLs compared with other loads. Therefore, as shown in Fig. 27, CPLs have behavior as a negative impedance, which is known as INR. Thus, the relation between voltage and current is given by

$$R = \frac{\Delta V_{CPL}}{\Delta I_{CPL}} = -\frac{P}{I^2} \tag{36}$$

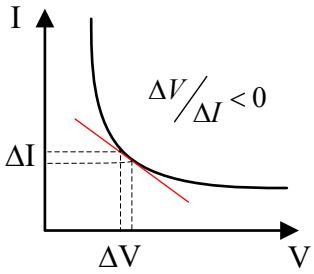

Fig. 27. *V-I* curve of CPLs (Figure from JP2).

The value of *R* is assigned by a negative sign, and it behaves as positive feedback. Thus, the current in a CPL increases when the voltage of the CPL terminal decreases. This has an impact on the impedance-based fault location methods, such as distance relays, since, relays measure a lower impedance, then the estimated distance will be higher than a real location. For instance, as shown in Fig. 28, if a relay is installed at bus A. and the fault has occurred between C and D, the resistance seen by the relay will be

$$R_{Seen} = R_{AB} + R_{BC} + R_{CF} + R_{fault} \tag{37}$$

$$R_{Seen} = \frac{V_{AB}}{I_{AB}} + \frac{V_{BC}}{I_{BC}} + \frac{V_{CF}}{I_{CF}} + \frac{V_F}{I_F} \tag{38}$$

$$I_{AB} = I_{CPL} + I_{BC} \tag{39}$$

According to the aforementioned equations, during the fault and voltage drop, the CPL current will increase, and it increases the observed impedance of distance relay. Therefore, a special protection system is essential for DC Microgrids with high penetration of CPLs.

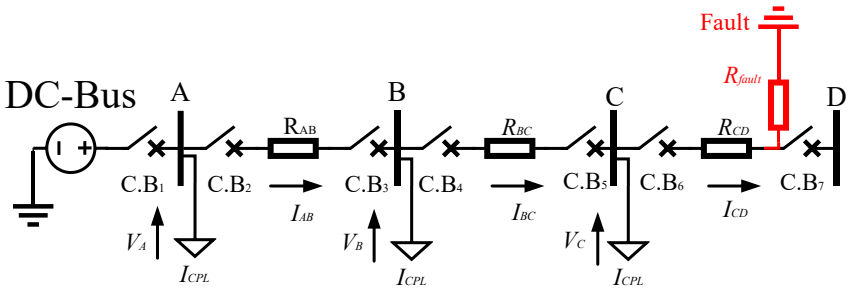

Fig. 28. A radial branch equipped with CPLs (Figure from JP5).

The negative impedance behavior of CPLs and its model is shown in Fig. 29. Thus, it leads to an increase in fault current in a short period, which provides problems on the operation and stability of different components in DC Microgrids. Therefore, the value of the current of CPLs can be calculated by

$$f(V_{CPL}) = I_{CPL} = \frac{P_{CPL}}{V_{CPL}} \tag{40}$$

where the value of P_{CPL} is constant, and the value of V_{CPL} dropping during the fault. Then the value of fault current in CPLs can be given as a time-variant equation

$$I_{CPL} = \frac{P_{CPL} e^{\alpha t} \omega}{V_0 \omega_0 \sin(\omega t + \beta) - \frac{I_0}{C} \sin(\omega t)} \tag{41}$$

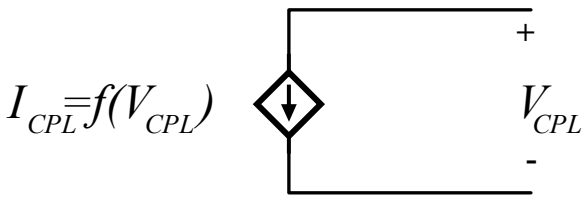

Fig.29. The model of CPL during capacitor discharge (Figure from JP2).

4.1.2. CPL Fault Resistance Estimation Method

In DC systems, after occurring the fault, the current immediately starts to increase, and the magnitude and peak time depend on the fault resistance. Moreover, for proposing an accurate fault location method, the estimation of fault resistance is essential. Therefore, the first step is estimating fault resistance. During the fault, the power flow from the relay side can be divided into three parts, the power consumption of fault resistance, CPLs, and power losses as

$$P_{relay} = P_{cable} + P_{CPLs} + P_{fault} \tag{42}$$

The value of power losses of cables is unknown, and the CPL power consumptions are known. The value of P_{relay} is measured by sensors in relay place. Therefore, (32) has two unknowns, P_{fault} and P_{cable}, and it can be rewritten as

$$P_{relay} = P_{CPLs} + R_{cable}\frac{L_C}{R_C}\frac{dI_{fault}}{dt}I_{fault} + (R_{fault} + R_{cable})I_{fault}^2 \tag{43}$$

where I_{fault} is measured by the sensor at the relay, however, the fault current at relay location is different from the actual fault current at the faulty point. Thus, the fault current at the faulty point is the difference between measured and loads current. The values of power in terms of fault current is

$$\begin{aligned} P_{relay(t1)} &= A + BI_{fault(t1)} + CI_{fault(t1)}^2 \\ P_{relay(t2)} &= A + BI_{fault(t2)} + CI_{fault(t2)}^2 \\ &\vdots \\ P_{relay(tn)} &= A + BI_{fault(tn)} + CI_{fault(tn)}^2 \end{aligned} \tag{44}$$

where the value of *A, B,* and *C* are given by:

$$A = P_{CPLs},\ B = R_{cable}\frac{L_C}{R_C}\frac{dI_{fault}}{dt},\ C = R_{fault} + R_{cable} \tag{45}$$

where $P_{relay(t1)}$, $P_{relay(t2)}$, … , $P_{relay(tn)}$ is the sampled value of power, $\Delta t = t_2 - t_1$ is the sampling interval, and in relay place, $I_{fault(t1)}$, $I_{fault(t2)}$, …, $I_{fault(tn)}$ are the sampled fault currents at relay place. To find the cable and fault resistances, the least square (LS) techniques is formulated as

$$[k][x] = [m] \tag{46}$$

$$[k] = \begin{bmatrix} n & \sum_1^n I_{fault_i} & \sum_1^n I_{fault_i}^2 \\ \sum_1^n I_{fault_i} & \sum_1^n I_{fault_i}^2 & \sum_1^n I_{fault_i}^3 \\ \sum_1^n I_{fault_i}^2 & \sum_1^n I_{fault_i}^3 & \sum_1^n I_{fault_i}^4 \end{bmatrix}, [m] = \begin{bmatrix} \sum_1^n P_{relay} \\ \sum_1^n P_{relay} I_{fault_i} \\ \sum_1^n P_{relay} I_{fault_i}^2 \end{bmatrix} \tag{47}$$

[x] is the column matrix of the *A*, *B*, and *C*. Thus, the value of *[x]*, and P_{cable} determined by

$$[x] = [k]^{-1}[m] \tag{48}$$

Consequently, the value of the fault resistance is obtained by

$$R_{fault} = \frac{P_{fault}}{I_{fault}^2} \tag{49}$$

The proposed is installed at the mainline, as Fig. 28, at the Bus A. The settings of the proposed scheme are based on the relation of the slope of fault current and fault resistance. In pre-fault conditions, a *ΔI/Δt-R* curve is designed based on the locations of fault, as shown in Fig. 30. Therefore, Fig. 30 represents the performance of fault current against fault resistance. The reduction trends of Fig. 30 proves the opposite relation between fault resistance and *ΔI/Δt*.

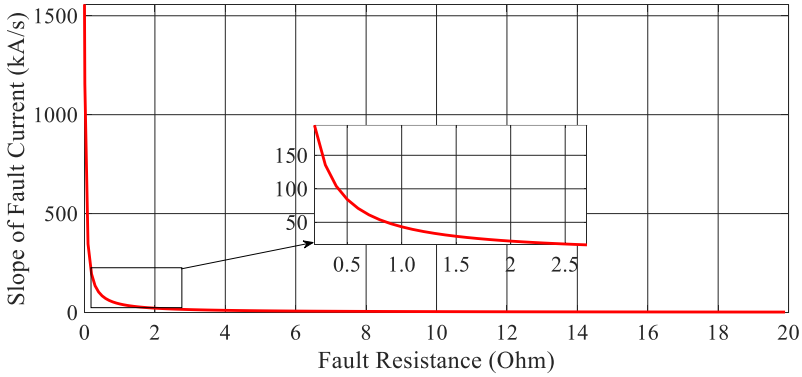

Fig. 30. The slope of fault current - fault resistance curve (Figure from JP2).

During a fault, the sensors measure the slope of fault current, voltage, and current, then, the value of fault resistance is estimated, and by using it, the location of the fault will be determined. Afterward, the trip signal will be sent to the C.B of the faulted CPL. The flowchart of the proposed scheme is represented in Fig. 31.

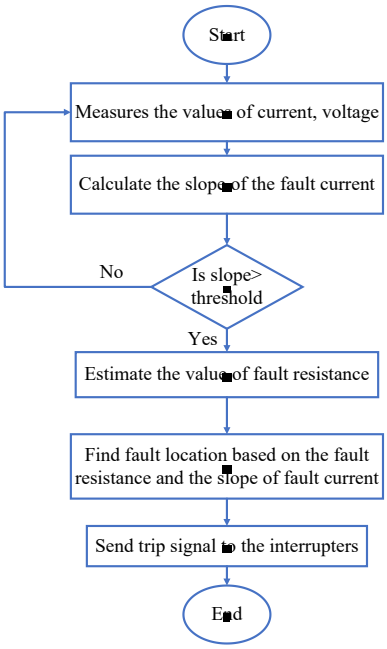

Fig. 31. The flowchart of the proposed method (Figure from JP2).

4.1.3. Experimental Results of CPL Fault Location Scheme

The validation of the local CPL protection system has been investigated in an experimental setup. Fig. 32 represents the fault current seen by relay during a fault with fault resistance of 11.9 Ω. As can be seen in Fig. 32, the measured value has noise, but, this is only the sensors' noise, and the communication noise is removed in this method. At Fig. 33, the fault currents for three different fault resistances are shown. Based on this figure, by increasing the fault resistance from 11.5 Ω to 13.8 Ω, the fault current is reduced from 3.68 A to 3.2 A. The slope of fault current for faults with fault resistances of 11.5 Ω, 12.1 Ω, and 13.8 Ω are 35 A/s, 34.3 A/s, and 33.1 A/s, respectively. The values of errors are defined in Table 5. As expected, by increasing the fault resistance, the accuracy will decrease by 4%. On the other hand, in terms of fault location estimation, during a CPL fault with 12.32 Ω, the maximum error will be 3.2%. As can be seen from Table 5, although the fault resistance of a

fault in line at 200 m is higher than CPL fault at 400 m, the error of line fault is lower than CPL fault. The reasons for that are, firstly, the higher distance of CPL fault, and second the INR impact of CPLs. However, the proposed method accurately locates the CPL fault during both HIFs and LIFs.

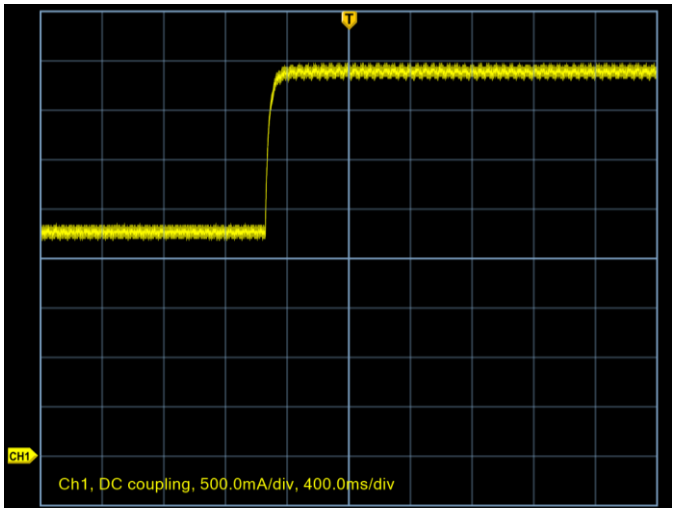

Fig. 32. The fault current of the main line during DC Motor fault (Figure from JP2).

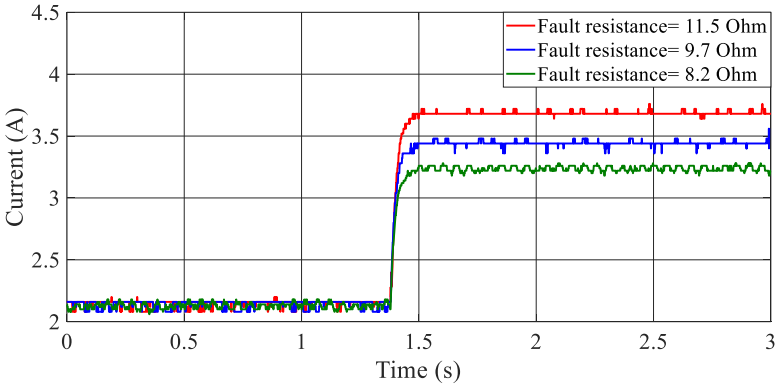

Fig. 33. Current for three different faults at CPL (Figure from JP2).

Table 5. Table from JP2, experimental fault location results of the proposed method

Faulty component	Actual fault resistance (Ω)	Fault location (m)	Calculated fault resistance (Ω)	Error (%)
DC Motor	19.84	600	19.04	4.04%
CPL	14.68	400	15.32	4.35%
DC load	15.21	200	14.68	3.48%
Line	12.63	200	12.47	1.26%
Faulty component	**Actual fault location (m)**	**Fault resistance (Ω)**	**Calculated fault location (m)**	**Error (%)**
CPL	600	9.76	581	3.07%
CPL	400	12.32	382	3.20%
Line	200	14.87	206	3.09%
Line	200	12.63	203	1.50%

4.2. Local Fault Location Based on Parameter Estimation Technique

The proposed fault location scheme consists of a current sensor and a localized intelligent electronic device (LIED), where they are installed at each line to determine the distance of fault at each line segment. Conventional existing schemes use the current and voltage data of the faulty line by using communication channels. In this proposed scheme, only the current of one end of the line segment is measured. Thus, the total size and cost of the fault location system will reduce, and the concerns related to noise and delay will be minimized. After isolation of fault by SSCBs, the equivalent circuit will be an RLC, as shown in Fig. 34. Thus, the proposed LIED starts to samples the current magnitude and direction to also locate the internal and external faults.

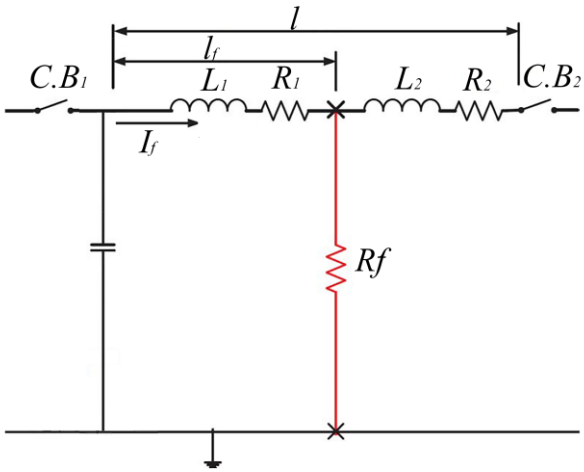

Fig. 34. Structure of faulty line segment after isolation (Figure from JP4).

The proposed fault location scheme only requires the local data of one side of the line segment. After isolating the fault by SSCBs, the performance of the faulty line will change to a equivalent RLC circuit. Thus, the LIED starts to measure the line current and during this stage, the equivalent circuit of the system is represented in Fig. 34. Once the SSCBs isolated the line, an RLC loop is formed, and the current of this loop is calculated as follows:

$$\frac{d^2 i_f(t)}{dt^2} + \frac{R_1 + R_f}{L_1}\frac{di_f(t)}{dt} + \frac{1}{L_1 C} i_f(t) = 0 \tag{50}$$

where R_1 and L_1 are the resistance and inductance of the line between LIED and fault location, respectively. $i_f(t)$ is the fault current, C is the capacitor of the inverter, and R_f is the fault resistance. Therefore, the $i_f(t)$ value in terms of the time can be determined by

$$i_f(t) = e^{-\alpha t}(D\cos(\omega t) + E\sin(\omega t)) \tag{51}$$

where ω and α can be calculated by

$$\begin{cases} \alpha = \dfrac{R_1 + R_f}{2L_1} \\ \omega = 0.5\sqrt{\dfrac{(R_1 + R_f)^2}{L_1^2} - \dfrac{4}{L_1 C}} \end{cases} \tag{52}$$

Since there are four unknown parameters in (41), more generate equations are essential to determine the unknown parameters. Thus, by using Taylor series, (41) is rewritten by neglecting higher-order terms by

$$i_f(t) = P_1 t^3 + P_2 t^2 + P_3 t + P_4 \tag{53}$$

where,

$$\begin{cases} P_1 = \dfrac{D}{6}(2\alpha\omega^2 - \alpha^3 - \alpha^2\omega) + \dfrac{E}{6}(3\alpha^2\omega - \omega^3) \\ P_2 = \dfrac{D}{2}(\alpha^2 - \omega^2) - E\alpha\omega \\ P_3 = -D\alpha + \omega E \\ P_4 = D \end{cases} \tag{54}$$

Consequently, the LIED needs the current measured with only four samples to calculate the values of P_1, P_2, P_3, and P_4 based on the underdamped current, as shown in Fig. 35, to a cubic equation. Solving (44) will give the values of ω, α, E, and D. Therefore, by substitution of ω, α, E, and D into (42), the values of L_1, R_f, and R_1 will be calculates. Moreover, for determining L_1 and R_1, the $R_s d$ and $L_s d$ should be replaced with them, where d is the fault location, L_s and R_s are the inductance and resistance of each line meter, respectively.

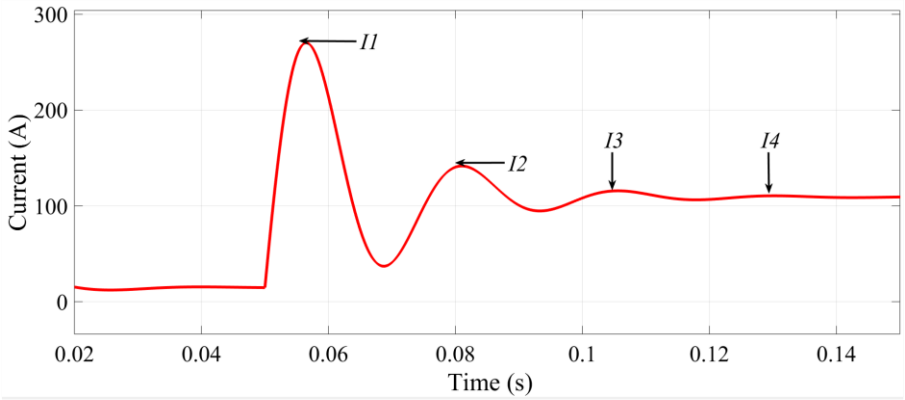

Fig. 35. Probe current response for different sample times (Figure from JP4).

4.2.1. Experimental Results of Proposed Fault Estimation Scheme

Fig. 36 (a) and (b) represents the experimental results of a HIF with fault resistance of 2 Ω and 3 Ω at 2 km, and 1 km distance from the LIED, respectively. The fault current magnitudes is 5.84 A for fault at 2 km, and 4.81 A for fault at 1 km, and they are damped after approximately 200 ms.

By using the proposed scheme, the fault distances are calculated for different fault conditions. These values are shown in Table 6. The maximum error value is 2.23%, and it validates the effectiveness of the proposed method.

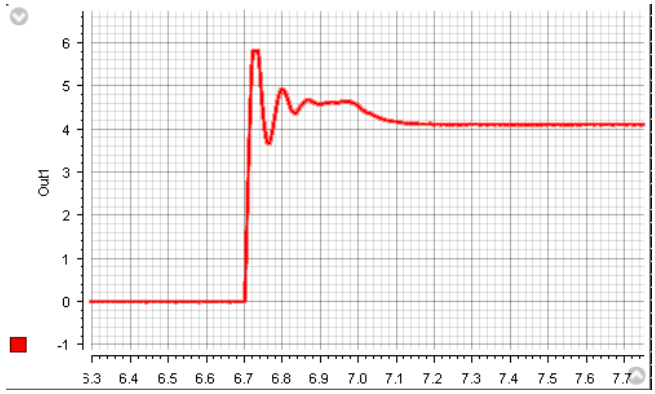

(a)

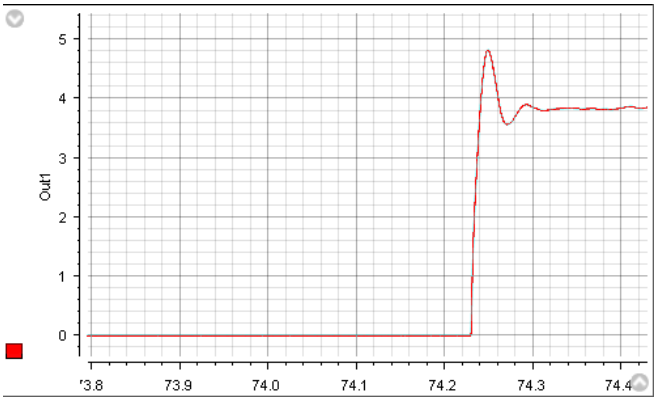

(b)

Fig. 36. The fault current of the LIED at one end of line for fault resistance of (a) 2 Ωs with 2 km (b) 3 Ωs with 1 km distance from LIED (Figure from JP4).

Table 6. Table from JP4, the results of fault location estimation for experimental tests

Fault resistance (Ω)	Actual fault location (m)	Estimated fault location (m)	Error (%)
1.4	1000	986	1.36
2.2	1000	985	1.48
3.2	1000	983	1.66
3.0	2000	1967	1.64
4.8	2000	1965	1.74
5.3	2000	1964	1.79
5.5	3000	2939	2.03
6.0	3000	2936	2.11
6.2	3000	2933	2.23

4.3. Proposed Fault Location Scheme by Using Support Vector Machines (SVMs)

The SVM-based fault location method is proposed in this section. The diagram of the different machine learning methods and their applications on fault location is presented in Fig. 37. The features used for developing a fault location estimator is based on the derivative of the current waveform over time *di/dt*, the maximum amplitude of fault current (*I*), and cable resistance (*R*). To train machine learning models, the distributed data are randomly into a testing parts (20%) and training data set (80%). The feature model of the whole data based on *di/dt* respect to *R* and *I* and respect to *I* are illustrated in Fig. 38 (a) and (b). It is concluded that the quadratic support vector machine (QSVM) [45] and fine k-nearest neighbor algorithm (KNN) [46] have the highest accuracy to estimate the locations of the faults.

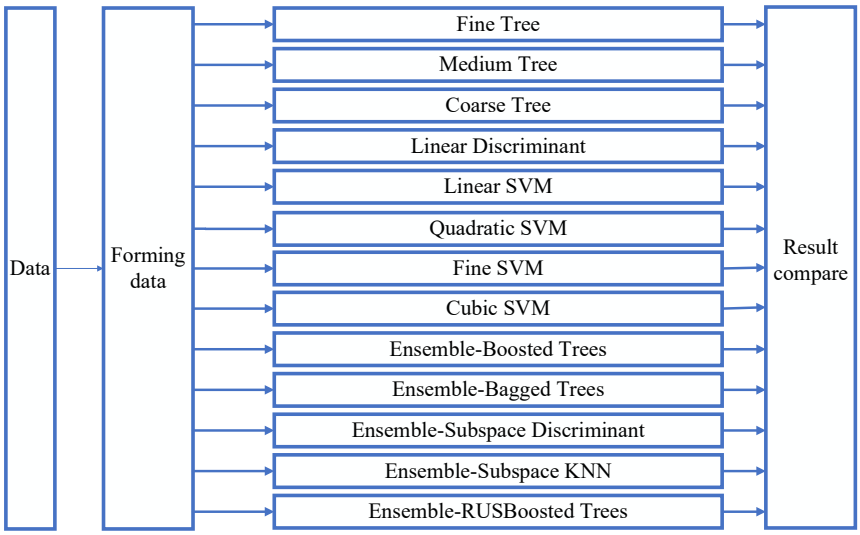

Fig. 37. The diagram of the proposed study for prediction of fault locations (Figure from JP6).

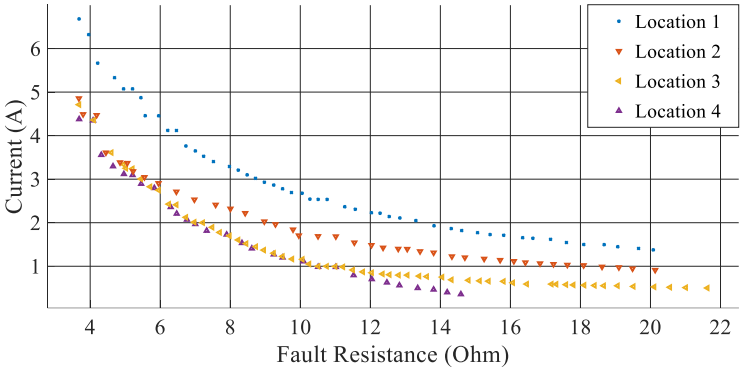

(a)

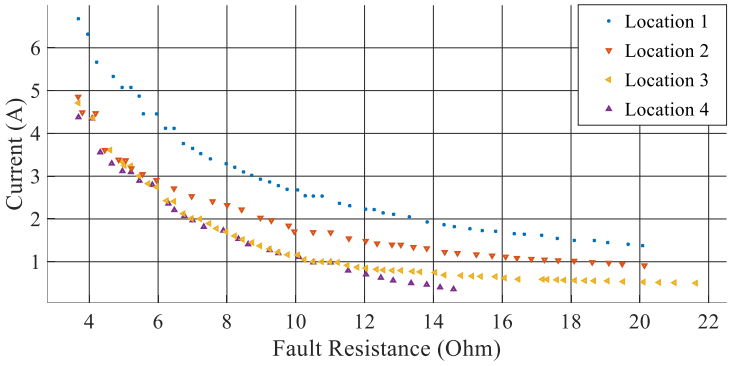

(b)

Fig. 38. The feature space model of faults according to (a) *I-di/dt*. (b) *R-I* (Figure from JP6).

The evaluation of the proposed scheme has been investigated in terms of the fault location accuracy during LIFs and HIFs. As shown in Fig. 39, different machine learning techniques, namely, SVM, ensemble learning, linear discriminant, and quadratic discriminant are investigated to find the optimum technique. It has been found that KNN and SVM methods have the best accuracy and ensemble learning has the lowest accuracy. The results of the developed techniques are presented in Fig. 39. Fig. 40 (a) and (b) represent the performance of SVM and quadratic discriminant techniques. It can be seen that the SVM classify successfully the features from the test data set without any mistakes. However, in quadratic discriminant, some of the features have

not been assigned to the right class, which is represented with a cross sign in fig 40 (a).

Fine Tree	Accuracy:80.6%
Medium Tree	Accuracy:80.6%
Coarse Tree	Accuracy:75.0%
Linear Discriminant	Accuracy:72.2%
Quadratic Discriminant	Accuracy:97.2%
Linear SVM	Accuracy:94.4%
Quadratic SVM	Accuracy:100%
Fine KNN	Accuracy:100%
Cubic KNN	Accuracy:94.4%
Boosted Trees	Accuracy:33.3%
Bagged Trees	Accuracy:97.2%
Subspace Discriminant	Accuracy:61.1%
Subspace KNN	Accuracy:66.7%
RUSBoosted Trees	Accuracy:94.4%

Fig. 39. The comparison errors of different machine learning methods (Figure from JP6).

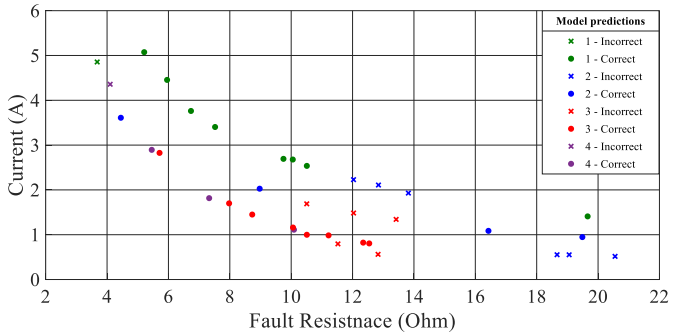

(a)

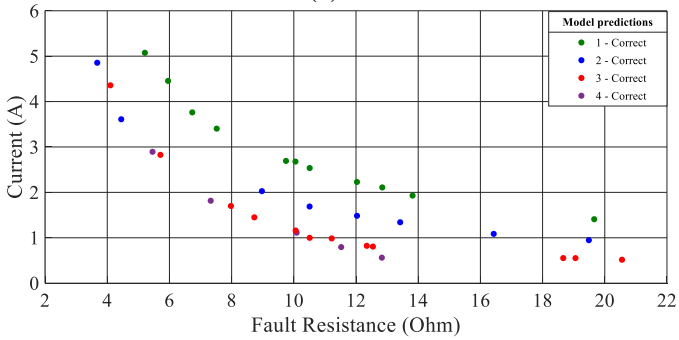

(b)

Fig. 40. The performance of (a) quadratic discriminant and (b) SVM algorithms (Figure from JP6).

The proposed scheme only requires the measured current of one side, and the derivative and magnitude of the fault current are extracted for all cases to design the fault location relay. For example, for a fault at t= 8.2 s, fault location of 400m, with fault resistance of 3.2 Ω, the fault current characteristic is depicted in Fig. 41. In this case, since the $\alpha^2<\omega_0^2$, the fault current has an underdamped nature with a peak value of 6.27 A, and the slope of 734 A/s. This high value of slope proves the low rise time in DC systems. Therefore, a high sampling rate is essential in DC systems. Moreover, the inequality $\alpha^2<\omega_0^2$ can be written as

$$4L^2C^2 < 4 - R^2C^2 \tag{55}$$

Thus, by increasing the value of fault resistance, the value of $4\text{-}R^2C^2$ reduces, and the fault current will have an overdamped performance, since $\alpha^2>\omega_0^2$.

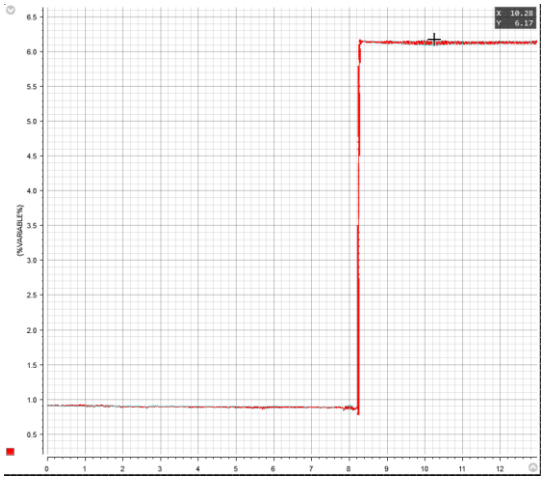

Fig. 41. The fault current performance for a LIF (Figure from JP6).

Table 7 presents the results of the estimated HIF location by the proposed technique using SVM for estimating four possible faulty locations in a range

of HIF resistances. The minimum fault location and resistance estimation error is approximately 100%, then the results of the proposed scheme to estimates the location of HIFs and LIFs in DC Microgrids are excellent.

To investigate the performance of the proposed method during noise and bad calibration input data, all measured values are multiplied by a normally distributed random number with zero mean and 1%, standard deviation, and for considering bad calibration, the measured magnitudes are multiplied by 1.05. The results are shown in Table 8.

Tables 8 show that the errors of fault resistance and location estimation in noisy situations. The average error for fault without noise is 1.82 %, and it increases slightly to 1.94% for bad calibration and it remains acceptable.

Table 7. Table from JP6, results for fault location using proposed scheme

Actual fault location (m)	Actual fault resistance (Ω)	*di/dt*	Error (%)
0	6.215	809.6	1.51
400	3.678	682.29	4.13
400	16.847	180.10	2.36
800	7.214	217.02	2.10
800	18.105	86.71	1.40
1200	9.495	19.02	0.33
1200	13.807	7.87	0.92

Table 8. Table from JP6, results for fault location using proposed scheme with noise generated (0,1%) and bad calibration in sensor

Actual fault location (m)	Actual fault resistance (Ω)	*di/dt*	Error (%)
0	6.215	842.0360	0.18
400	3.678	709.6254	4.27
400	16.847	187.3156	5.13
800	7.214	225.7147	2.51
800	18.105	90.1840	0.64
1200	9.495	19.7820	0.255
1200	13.807	8.1853	0.60

4.3.1. Comparison of the Proposed Fault Location Methods and Existing Works

The proposed fault location methods are compared with [47]-[51]. The suggested methods in [47] and [49] require additional equipment for the protection of DC microgrids. In [49] and [47], an inductance based and RLC based fault location estimator is proposed and installed both ends of the under-protected line, respectively. After the fault, the stored energy of the fault location device is discharge in the circuit to estimate the fault location by using the measured values of current. However, the maximum error and fault resistance of [49] are 13% and 10 Ω, respectively. Moreover, in [47], these maximum values are 8% and 2 Ω, respectively. However, both methods require a communication channel, which increases the cost of the system.

In [48] and [50], the location of the fault in DC microgrids is estimated by solving transient equations and neural networks, respectively. In both schemes, the measured values of voltage and current of both sides of the line segment are sent by communication links to protection function. However, the

fault location of HIFs is considered in [50]. The suggested method of [51] is designed without utilizing communication links.

Table 9. Comparison of the proposed scheme with other existing DC fault location methods

Method	Cost	Maximum Error	Maximum fault resistance	Communication links	Topology
[47]	Extremely high	8%	2 Ω	Yes	Ring
[48]	Moderate	6%	2 Ω	Yes	Radial
[49]	Extremely high	13%	10 Ω	Yes	Ring
[50]	Extremely High	2%	2.4 Ω	Yes	Ring
[51]	Moderate	4.7%	1 Ω	No	Ring
Proposed parameter estimation method	Low	5%	20 Ω	No	Ring
Proposed CPL protection method	Low	6%	6 Ω	No	Radial
Proposed parameter SVM method	Low	5%	20 Ω	No	Ring

The proposed methods use a local structure without using any additional equipment, then, the cost of these methods is minimized. All schemes are equipped with HIF locators, however, the maximum fault resistance of the CPL protection method is limited to 6 Ω. In addition, the proposed parameter estimation method and SVM technique can locate faults in both ring and radial systems, however, the CPL protection is designed for radial systems. Moreover, the errors of all proposed method are in the same range, at 5%, which prove the high accuracy of these proposed methods.

Chapter 5

Conclusion and Future Work

The conclusion and future works of this research based on papers are presented in this section

5.1. Conclusion

The previous DC microgrid fault detection and location schemes are effective theoretically, however, they almost require communication links, or cannot be effective during HIFs. Consequently, these methods are costly to be implemented in practical DC systems. Thus, in this work, localized fault location and detection schemes were proposed to protect the DC Microgrid and DC Microgrid clusters without using the communication channels. Therefore, the failure probability, cost, noise, and delay due to the communication channels are minimized. The obtained results proved the accuracy of the proposed schemes for different fault distances and resistances and scenarios. The proposed methods are examined in scaled hardware setup to validate the accuracy of these methods. Finally, the performance of the proposed approaches was investigated by performing simulations in MATLAB/Simulink environment, and the results were verified experimentally by experimental setup tests during the HIFs and LIFs to prove the authenticity, accuracy, and effectiveness of the proposed schemes on different conditions. Furthermore, the proposed protection strategies were compared with other existing methods, and the comparative results define that the proposed schemes have a lower error, and higher effectiveness compared to the other protection methods.

5.3.Future Work

In this work, the fault detection and location method for DC Microgrids and clusters are proposed, however, some future works can be applied to this work:

- Improve the model of protection system by taking into account the uncertainties of renewable energy resources.
- Development of a protection system for an special application such as maritime DC Microgrid or aircrafts.
- Development of an international standard for the protection design of DC Microgrids.
- Investigate the protection issues of hybrid AC/DC Microgrids.
- Analyzing the impact of different converter structures on the protection of DC systems.

References

[1]. Brearley, B.J., Raja Prabu, R.: 'A review on issues and approaches for microgrid protection', Renew. Sustain. Energy Rev., 2017, 67, pp. 988–997.

[2]. Lakshmi M, Hemamalini S. Nonisolated high gain DC–DC converter for DC microgrids. IEEE Transactions on Industrial Electronics. 2017 Jul 31;65(2):1205-12.

[3]. Manohar, P., Ahmed, W.: 'Superconducting fault current limiter to mitigate the effect of DC line fault in VSC-HVDC system'. 2012 Int. Conf. on Power, Signals, Controls and Computation (EPSCICON), Thrissur, Kerala, India, 2012.

[4]. de Oliveira, T.R., Bolzon, A.S., Donoso-Garcia, P.F.: 'Grounding and safety considerations for residential DC microgrids'. IECON 2014 – 40th Annual Conf. of the IEEE Industrial Electronics Society, Dallas, TX, USA, 2014.

[5]. Amamra, S.-A., Ahmed, H., El-Sehiemy, R.A.: 'Firefly algorithm optimized robust protection scheme for DC microgrid', Electr. Power Compon. Syst., 2017, 45, (10), pp. 1141–1151

[6]. Cuzner, R., Venkataramanan, G.: 'The status of DC micro-grid protection'. Proc. IEEE Industry Applications Society Annual Meeting (IAS), Edmonton, AB, Canada, October 2008, pp. 1–8.

[7]. Elsayed, A.T., Mohamed, A.A., Mohammed, O.A.: 'DC microgrids and distribution systems: an overview', Electr. Power Syst. Res., 2015, 119, pp. 407–417.

[8]. Jin, Z., Savaghebi, M., Vasquez, J.C., et al.: 'Maritime DC microgrids-a combination of microgrid technologies and maritime onboard power system for future ships'. 2016 IEEE Eighth Int. Power Electronics and Motion Control Conf. (IPEMC-ECCE Asia), Hefei, China, 2016.

[9]. Jin Z, Sulligoi G, Cuzner R, Meng L, Vasquez JC, Guerrero JM. Next-generation shipboard dc power system: Introduction smart grid and dc microgrid technologies into maritime electrical netowrks. IEEE Electrification Magazine. 2016 May 30;4(2):45-57.

[10]. Son YK, Lee SY, Ko S, Kim YW, Sul SK. Maritime DC Power System with Generation Topology Consisting of Combination of Permanent Magnet Generator and Diode Rectifier. IEEE Transactions on Transportation Electrification. 2020 May 5.

[11]. Peña-Aguirre JC, Barranco-Gutiérrez AI, Padilla-Medina JA, Espinosa-Calderon A, Pérez-Pinal FJ. Fuzzy Logic Power Management Strategy for a Residential DC-Microgrid. IEEE Access. 2020 Jun 24;8:116733-43.

[12]. Kaur R, Krishnasamy V, Kandasamy NK. Optimal sizing of wind–PV-based DC microgrid for telecom power supply in remote areas. IET Renewable Power Generation. 2018 Feb 8;12(7):859-66.

[13]. Shen L, Cheng Q, Cheng Y, Wei L, Wang Y. Hierarchical control of DC micro-grid for photovoltaic EV charging station based on flywheel and battery energy storage system. Electric Power Systems Research. 2020 Feb 1;179:106079.

[14]. Dong C, Gao Q, Xiao Q, Yu X, Pekař L, Jia H. Time-delay stability switching boundary determination for DC microgrid clusters with the distributed control framework. Applied Energy. 2018 Oct 15;228:189-204.

[15]. Baghaee HR, Mirsalim M, Gharehpetian GB, Talebi HA. A decentralized power management and sliding mode control strategy for hybrid AC/DC microgrids including renewable energy resources. IEEE transactions on industrial informatics. 2017 Mar 3.

[16]. P. P. Barker and R. W. De Mello, "Determining the impact of distributed generation on power systems. i. radial distribution systems," in Proc. IEEE Power Engineering Society Summer Meeting, July 2000, vol. 3, pp. 1645–1656.

[17]. Kamel, R.M., Chaouachi, A., Nagasaka, K.: 'Comparison the performances of three earthing systems for micro-grid protection during the grid connected mode', Smart Grid Renew. Energy, 2011, 2, (03), p. 206

[18]. Mirsaeidi, S., Said, D.M., Mustafa, M.W., et al.: 'Progress and problems in micro-grid protection schemes', Renew. Sustain. Energy Rev., 2014, 37, pp. 834–839.

[19]. Corzine KA, Ashton RW. A new Z-source DC circuit breaker. IEEE Transactions on Power Electronics. 2011 Dec 5;27(6):2796-804.

[20]. Baran, M.E., Mahajan, N.R.: 'Overcurrent protection on voltage-source converter-based multiterminal DC distribution systems', IEEE Trans. Power Deliv., 2007, 22, (1), pp. 406–412.

[21]. Malekpour, A.R., Niknam, T., Pahwa, A., et al.: 'Multi-objective stochastic distribution feeder reconfiguration in systems with wind power generators and fuel cells using the point estimate method', IEEE Trans. Power Syst., 2013,28, (2), pp. 1483–1492.

[22]. Park, J. D., Candelaria, J., Ma, L., & Dunn, K. "DC ring-bus microgrid fault protection and identification of fault location." IEEE transactions on Power delivery 28.4 (2013): 2574-258.

[23]. D. Kumar, F. Zare, and A. Ghosh, "DC microgrid technology: System architectures, AC grid interfaces, grounding schemes, power quality, communication networks, applications, and standardizations aspects," IEEE Access, vol. 5, pp. 12230-12256,2017.

[24]. Amamra, S.-A., Ahmed, H., El-Sehiemy, R.A.: 'Firefly algorithm optimized robust protection scheme for DC microgrid', Electr. Power Compon. Syst., 2017, 45, (10), pp. 1141–1151.

[25]. D. Salomonsson, S. Member, L. Söder, and A. Sannino, "Protection of Low-Voltage DC Microgrids," IEEE Trans. Power Del., vol. 24, no. 3, pp. 1045–1053, 2009.

[26]. M. Monadi, C. Koch-ciobotaru, A. Luna, J. I. Candela, and P. Rodriguez, “A Protection Strategy for Fault Detection and Location for Multi-Terminal MVDC Distribution Systems with Renewable Energy Systems,” in International Conference on Renewable Energy Research and Application (ICRERA), 2014, pp. 496–501.

[27]. S. D. A. Fletcher, P. J. Norman, S. J. Galloway, P. Crolla, and G. M. Burt, “Optimizing the roles of unit and non-unit protection methods within DC microgrids,” IEEE Trans. Smart Grid, vol. 3, no. 4, pp. 2079–2087, 2012.

[28]. Yang, J., Fletcher, J.E., O'Reilly, J.: ‘Short-circuit and ground fault analyses and location in VSC-based DC network cables’, IEEE Trans. Ind. Electron., 2012, 59, pp. 3827–3837.

[29]. Aly, M.M.A.M., El-Sayed, M.A.H.: ‘Enhanced fault location algorithm for smart grid containing wind farm using wireless communication facilities’, IET Gener. Transm. Distrib., 2016, 10, (9), pp. 2231–2239.

[30]. Park, J.-D., Candelaria, J.: ‘Fault detection and isolation in low-voltage DC bus microgrid system’, IEEE Trans. Power Deliv., 2013, 28, (2), pp. 779–787.

[31]. Li, W., Luo, M., Monti, A., et al.: ‘Wavelet based method for fault detection in medium voltage DC shipboard power systems’. 2012 IEEE Int. Instrumentation and Measurement Technology Conf. (I2MTC), Graz, Austria, 2012

[32]. De Kerf, K., Srivastava, K., Reza, M., et al.: ‘Wavelet-based protection strategy for DC faults in multi-terminal VSC HVDC systems’, IET Gener. Transm. Distrib., 2011, 5, (4), pp. 496–503.

[33]. D. K. J. S. Jayamaha, N. W. A. Lidula and A. D. Rajapakse, "Wavelet-Multi Resolution Analysis Based ANN Architecture for Fault Detection and Localization in DC Microgrids," in IEEE Access, vol. 7, pp. 145371-145384, 2019, doi: 10.1109/ACCESS.2019.2945397.

[34]. A. Meghwani, S. C. Srivastava, and S. Chakrabarti, “A Non-unit Protection Scheme for DC Microgrid Based on Local Measurements,” IEEE Trans. Power Deliv., vol. 32, no. 1, pp. 172–181, 2017.

[35]. R. Hu, J. Wang, A. R. Mills, E. Chong, and Z. Sun, "Detection and Classification of Turn Fault and High Resistance Connection Fault in Permanent Magnet Machines based on Zero Sequence Voltage," IEEE Trans. on Power Electronics, vol. 35, no. 2, pp. 1922-1933, February 2020.

[36]. P. Maragos, R. Schafer, “Morphological filters – part i: their set-theoretic analysis and relations to linear shift-invariant filters,” IEEE Trans. on Acoust Speech Signal Process, vol.35, no. 8, pp. 1153-1169, August 1987.

[37]. P. Maragos, R. Schafer, “Morphological filters – part i: their set-theoretic analysis and relations to linear shift-invariant filters,” IEEE Trans. on Acoust Speech Signal Process, vol.35, no. 8, pp. 1153-1169, August 1987.

[38]. S. Gautam, S.M. Brahma, “Overview of mathematical morphology in power systems – a tutorial approach,” in Proc. IEEE Power Engineering Society General Meeting, Calgary, Canada. 2009. p. 1–7.

[39]. E. Lavopa, P. Zanchetta, M. Sumner, and F. Cupertino, “Real time estimation of fundamental frequency and harmonics for active shunt power filter in aircraft electrical systems,” IEEE Trans. Ind. Electron., vol. 56, no. 8, pp. 2875–2884, Aug. 2009.

[40]. S. Dhar, R. K. Patnaik and P. K. Dash, "Fault Detection and Location of Photovoltaic Based DC microgrid Using Differential Protection Strategy," IEEE Trans. on Smart Grid, vol. 9, no. 5, pp. 4303-4312, September 2018.

[41]. P. Cairoli and R. A. Dougal, "Fault Detection and Isolation in Medium-Voltage DC microgrids: Coordination Between Supply Power Converters and Bus Contactors," IEEE Trans. on Power Electronics, vol. 33, no. 5, pp. 4535-4546, May 2018.

[42]. Y.M. Yeap, N. Geddada, K. Satpathi, and A. Ukil, “Time and Frequency Domain Fault Detection in VSC Interfaced Experimental DC Test System,” IEEE Trans. on Industrial Informatics, vol. 14, no. 10, pp. 4353-4364, October 2018.

[43]. K. Subramaniam and M. S. Illindala, "Intelligent Three Tie Contactor Switch Unit-Based Fault Detection and Isolation in DC Microgrids," in IEEE Transactions on Industry Applications, vol. 56, no. 1, pp. 95-105, Jan.-Feb. 2020.

[44]. D. K. J. S. Jayamaha, N. W. A. Lidula and A. D. Rajapakse, "Wavelet-Multi Resolution Analysis Based ANN Architecture for Fault Detection and Localization in DC Microgrids," in IEEE Access, vol. 7, pp. 145371-145384, 2019.

[45]. Dug Hun Hong and Changha Hwang, "Interval regression analysis using quadratic loss support vector machine," in IEEE Transactions on Fuzzy Systems, vol. 13, no. 2, pp. 229-237, April 2005, doi: 10.1109/TFUZZ.2004.840133.

[46]. Madeti SR, Singh SN. Modeling of PV system based on experimental data for fault detection using kNN method. Solar Energy. 2018 Oct 1;173:139-51.

[47]. R. Mohanty, U. S. M. Balaji, and A. K. Pradhan, “An accurate noniterative fault-location technique for low-voltage DC microgrid,” IEEE Trans. Power Del., vol. 31, no. 2, pp. 475–481, Apr. 2016.

[48]. S. Dhar, R. K. Patnaik and P. K. Dash, "Fault Detection and Location of Photovoltaic Based DC microgrid Using Differential Protection Strategy," in IEEE Transactions on Smart Grid, vol. 9, no. 5, pp. 4303-4312, Sept. 2018.

[49]. Y. Yang, C. Huang and Q. Xu, "A Fault Location Method Suitable for Low-Voltage DC Line," in IEEE Transactions on Power Delivery, vol. 35, no. 1, pp. 194-204, Feb. 2020.

[50]. Sharanya M, Devi MM, Geethanjali M. Fault Detection and Location in DC microgrid. In2018 National Power Engineering Conference (NPEC) 2018 Mar 9 (pp. 1-7). IEEE.

[51]. D. Wang, V. Psaras, A. A. S. Emhemed and G. M. Burt, "A Novel Fault Let-through Energy based Fault Location for LVDC Distribution Networks," in IEEE Transactions on Power Delivery, doi: 10.1109/TPWRD.2020.2998409.

ISSN (online): 2446-1636
ISBN (online): 978-87-7210-824-7 AALBORG UNIVERSITY PRESS